

## Article

# A reanalysis of the latest SH0ES data for $H_0$ : Effects of new degrees of freedom on the Hubble tension.

Leandros Perivolaropoulos<sup>1,†</sup>  and Foteini Skara<sup>1,‡</sup> 

<sup>1</sup> Department of Physics, University of Ioannina, 45110 Ioannina, Greece

† leandros@uoi.gr

‡ f.skara@uoi.gr

**Abstract:** We reanalyze in a simple and comprehensive manner the recently released SH0ES data for the determination of  $H_0$ . We focus on testing the homogeneity of the Cepheid+SnIa sample and the robustness of the results in the presence of new degrees of freedom in the modeling of Cepheids and SnIa. We thus focus on the four modeling parameters of the analysis: the fiducial luminosity of SnIa  $M_B$  and Cepheids  $M_W$  and the two parameters ( $b_W$  and  $Z_W$ ) standardizing Cepheid luminosities with period and metallicity. After reproducing the SH0ES baseline model results, we allow for a transition of the value of any one of these parameters at a given distance  $D_c$  or cosmic time  $t_c$  thus adding a single degree of freedom in the analysis. When the SnIa absolute magnitude  $M_B$  is allowed to have a transition at  $D_c \simeq 50\text{Mpc}$  (about 160Myrs ago), the best fit value of the Hubble parameter drops from  $H_0 = 73.04 \pm 1.04 \text{ km s}^{-1} \text{ Mpc}^{-1}$  to  $H_0 = 67.32 \pm 4.64 \text{ km s}^{-1} \text{ Mpc}^{-1}$  in full consistency with the Planck value. Also, the best fit SnIa absolute magnitude  $M_B^>$  for  $D > D_c$  drops to the Planck inverse distance ladder value  $M_B^> = -19.43 \pm 0.15$  while the low distance best fit  $M_B^<$  parameter remains close to the original distance ladder calibrated value  $M_B^< = -19.25 \pm 0.03$ . Similar hints for a transition behavior is found for the other three main parameters of the analysis ( $b_W$ ,  $M_W$  and  $Z_W$ ) at the same critical distance  $D_c \simeq 50\text{Mpc}$  even though in that case the best fit value of  $H_0$  is not significantly affected. When the inverse distance ladder constraint on  $M_B^>$  is included in the analysis, the uncertainties for  $H_0$  reduce dramatically ( $H_0 = 68.2 \pm 0.8 \text{ km s}^{-1} \text{ Mpc}^{-1}$ ) and the  $M_B$  transition model is strongly preferred over the baseline SH0ES model ( $\Delta\chi^2 \simeq -15$ ,  $\Delta\text{AIC} \simeq -13$ ) according to AIC and BIC model selection criteria.

**Keywords:** Hubble tension; cosmology; galaxies; Cepheid calibrators; gravitational transition; SH0ES data

## 1. Introduction

### 1.1. The current status of the Hubble tension and its four assumptions

Measurements of the Hubble constant using observations of type Ia supernovae (SnIa) with Cepheid calibrators by the SH0ES Team has lead to a best fit value  $H_0 = 73.04 \pm 1.04 \text{ km s}^{-1} \text{ Mpc}^{-1}$  [1] (hereafter R21). This highly precise but not necessarily accurate measurement is consistent with a wide range of other less precise local measurements of  $H_0$  using alternative SnIa calibrators [2–5], gravitational lensing [6–9], gravitational waves [10–14], quasars as distant standard candles [15], type II supernovae [16,17],  $\gamma$ –ray attenuation [18] etc. (for recent reviews see Refs. [19,20]). This measurement is based on two simple assumptions:

- There are no significant systematic errors in the measurements of the properties (period, metallicity) and luminosities of Cepheid calibrators and SnIa.
- The physical laws involved and the calibration properties of Cepheids and SnIa in all the rungs of the distance ladder are well understood and modelled properly.



**Citation:** Perivolaropoulos, L.; Skara, F. *title* *universe* **2022**, *1*, 0.

<https://doi.org/>

Academic Editor: Firstname  
Lastname

Received:

Accepted:

Published:

**Publisher's Note:** MDPI stays neutral with regard to jurisdictional claims in published maps and institutional affiliations.



**Copyright:** © 2022 by the authors. Licensee MDPI, Basel, Switzerland. This article is an open access article distributed under the terms and conditions of the Creative Commons Attribution (CC BY) license (<https://creativecommons.org/licenses/by/4.0/>).

This measurement however is at  $5\sigma$  tension (Hubble tension) with the corresponding measurement from *Planck* observations of the CMB angular power spectrum (early time inverse distance ladder measurement)  $H_0 = 67.36 \pm 0.54 \text{ km s}^{-1} \text{ Mpc}^{-1}$  [21] (see also Refs. [19,20,22–29] for relevant recent reviews). This inverse distance ladder measurement is also based on two basic assumptions:

- The scale of the sound horizon at the last scattering surface is the one calculated in the context of the standard cosmological model with the known degrees of freedom (cold dark matter, baryons and radiation) and thus it is a reliable distance calibrator.
- The evolution of the Hubble free expansion rate  $E(z) \equiv H(z)/H_0$  from the time of recombination (redshift  $z = z_{rec}$ ) until the present time ( $z = 0$ ) is the one predicted by the standard  $\Lambda$ CDM model as defined by the best fit Planck parameters (Planck18/ $\Lambda$ CDM) [21,30].

A wide range of approaches have been implemented in efforts to explain this Hubble tension (for reviews see Refs. [19,20,22,29,31–34]). These approaches introduce new degrees of freedom that violate at least one of the above four assumptions and may be classified in accordance with the particular assumption they are designed to violate.

Thus, early time sound horizon models introduce new degrees of freedom at the time just before recombination (e.g. early dark energy [31,35–46], radiation [47–50] or modified gravity [51–56]) to change the expansion rate at that time and thus decrease the sound horizon scale  $r_s$  (early time distance calibrator) to increase  $H_0$ , which is degenerate with  $r_s$ , to a value consistent with local measurements.

The mechanism proposed by these models attempts to decrease the scale of the sound horizon at recombination which can be calculated as

$$r_s = \int_0^{t_*} \frac{c_s(a)}{a(t)} dt = \int_{z_*}^{\infty} \frac{c_s(z)}{H(z; \rho_b, \rho_\gamma, \rho_c)} dz = \int_0^{a_*} \frac{c_s(a)}{a^2 H(a; \rho_b, \rho_\gamma, \rho_c)} da \quad (1)$$

where the recombination redshift  $z_*$  corresponds to time  $t_*$ ,  $\rho_b$ ,  $\rho_c$  and  $\rho_\gamma$  denote the densities for baryon, cold dark matter and radiation (photons) respectively and  $c_s$  is the sound speed in the photon-baryon fluid. The angular scale of the sound horizon is measured by the peak locations of the CMB perturbations angular power spectrum and may be expressed in terms of  $r_s$  as

$$\theta_s = \frac{r_s}{d_A} = \frac{H_0 r_s}{c \int_0^{z_*} \frac{dz'}{E(z')}} \quad (2)$$

where  $d_A$  is the comoving angular diameter distance to last scattering (at redshift  $z \approx 1100$ ) and  $E(z)$  is the dimensionless normalized Hubble parameter which for a flat  $\Lambda$ CDM model is given by

$$E(z) \equiv \frac{H(z)}{H_0} = \left[ \Omega_{0m} (1+z)^3 + (1-\Omega_{0m}) \right]^{1/2} \quad (3)$$

Eq. (2) indicates that there is a degeneracy between  $r_s$ ,  $H_0$  and  $E(z)$  given the measured value of  $\theta_s$ . A decrease of  $r_s$  would lead to an increase of the predicted value of  $H_0$  (early time models) and a late time deformation of  $E(z)$  could lead to an increase of the denominator of Eq. (2) leading also to an increase of  $H_0$  (late time models).

Early dark energy models have the problem of predicting stronger growth of perturbations than implied by dynamical probes like redshift space distortion (RSD) and weak lensing (WL) data and thus may worsen the  $\Omega_m$ - $\sigma_8$  growth tension [57–66] and reduce consistency with growth data and with other cosmological probes and conjectures [33,34,42–44,66–70]. Thus, a compelling and full resolution of the Hubble tension may require multiple (or other) modifications beyond the scale of the sound horizon predicted by  $\Lambda$ CDM cosmology. Even

though these models are severely constrained by various cosmological observables, they currently constitute the most widely studied class of models [37–39,45,71,72].

Late time  $H(z)$  deformation models introduce new degrees of freedom (e.g. modified gravity [73–76] dynamical late dark energy [77–85] or interacting dark energy with matter [79,86–90]) to deform  $E(z)$  at redshifts  $z \sim O(1)$  so that the present time value of  $H(z = 0) = H_0$  increases and becomes consistent with the local measurements. This class of models is even more severely constrained [78,91–99] by other cosmological observables (SnIa, BAO and growth of perturbations probes) which tightly constrain any deformation [100] from the Planck18/ $\Lambda$ CDM shape of  $E(z) \equiv H(z)/H_0$ .

The third approach to the resolution of the Hubble tension is based on a search for possible unaccounted systematic effects including possible issues in modelling the Cepheid data such as non-standard dust induced colour correction [101], the impact of outliers [102–104], blending effects, SnIa color properties [105] etc. There is currently a debate about the importance of these potential systematic effects [106–109].

A fourth approach related to the previous one is based on a possible change of the physical laws (e.g. a gravitational transition) during the past 200 Myrs ( $z \lesssim 0.01$ ) when the light of the Cepheid calibrator hosts was emitted [110–118]. In this context, new degrees of freedom should be allowed for the modeling of either Cepheid calibrators or/and SnIa to allow for the possibility of this physics change. If these degrees of freedom are shown not to be excited by the data then this approach would also be severely constrained. It is possible however that nontrivial values of these new parameters are favored by the data while at the same time the best fit value of  $H_0$  shifts to a value consistent with the inverse distance ladder measurements of  $H_0$  using the sound horizon at recombination as calibrator. In this case [112], this class of models would be favored especially in view of the severe constraints that have been imposed on the other three approaches.

The possible new degrees of freedom that could be allowed in the Cepheid+SnIa modeling analysis are clearly infinite but the actual choices to be implemented in a generalized analysis may be guided by three principles: *simplicity, physical motivation and improvement of the quality of fit to the data*.

In a recent analysis [112] using a previous release of the SH0ES data [119–121] we showed that a physically motivated new degree of freedom in the Cepheid calibrator analysis allowing for a transition in one of the Cepheid modelling parameters  $R_W$  or  $M_W$ , is mildly favored by the data and can lead to a reduced best fit value of  $H_0$ . Here we extend that analysis in a detailed and comprehensive manner, to a wider range of transition degrees of freedom using the latest publicly available SH0ES data described in R21.

## 1.2. The new SH0ES Cepheid+SnIa data

The new Cepheid+SnIa data release and analysis from the SH0ES collaboration in R21 includes a significant increase of the sample of SnIa calibrators from 19 in Ref. [119] to 42. These SnIa reside in 37 hosts observed between 1980 and 2021 in a redshift range  $0.0015 \lesssim z < 0.011$ . These SnIa are calibrated using Cepheids in the SnIa host galaxies. In turn, Cepheid luminosities are calibrated using geometric methods in calibrator nearby galaxies (anchors). These anchor galaxies include the megamaser host NGC 4258<sup>1</sup>, the Milky Way (MW) where distances are measured with several parallaxes, and the Large Magellanic Cloud (LMC) where distances are measured via detached eclipsing binaries [120] as well as two supporting anchor galaxies (M31 [123] and the Small Magellanic Cloud (SMC). These supporting galaxies are pure Cepheid hosts and do not host SnIa but host large and well measured Cepheid samples. However,

<sup>1</sup> At a distance  $D = 7.6\text{Mpc}$  [122] NGC 4258 is the closest galaxy, beyond the Local Group, with a geometric distance measurement.

geometric measurements of their distances are not so reliable and thus are not directly used in the analysis<sup>2</sup>. The calibrated SnIa in the Hubble flow ( $z \gtrsim 0.01$ ) are used to measure  $H_0$  due to their high precision (5% in distance per source) and high luminosity which allows deep reach and thus reduces the impact of local velocity flows.

The new SH0ES data release includes a factor of 3 increase in the sample of Cepheids within NGC 4258. In total it has 2150 Cepheids in SnIa hosts<sup>3</sup>, 980 Cepheids in anchors or supporting galaxies<sup>4</sup>, 42 SnIa (with total 77 lightcurve dataset measurements) in 37 Cepheid+SnIa hosts with redshifts  $0.0015 \lesssim z < 0.011$  and 277 SnIa in the Hubble flow in the redshift range  $0.023 < z < 0.15$ . In addition 8 anchor based constraints (with uncertainties included) constrain the following Cepheid modeling parameters:  $M_W$  (the Cepheid absolute magnitude zeropoint),  $b_W$  (the slope of the Cepheid Period-Luminosity P-L relation),  $Z_W$  (the slope of the Cepheid Metallicity-Luminosity M-L relation), a zeropoint parameter  $zp$  used to refine the Cepheid P-L relation by describing the difference between the ground and HST zeropoints in LMC Cepheids ( $zp$  is set to 0 for HST observations), the distance moduli of the anchors NGC 4258 and LMC and a dummy parameter we call  $X$  which has been included in the R21 data release and is set to 0 with uncertainty  $10^{-9}$ <sup>5</sup>.

The parameters fit with these data include the four modeling parameters  $M_W$ ,  $b_W$ ,  $Z_W$ ,  $M_B$  (the SnIa absolute magnitude), the 37 distance moduli of SnIa/Cepheid hosts, the distance moduli to the 2 anchors (NGC 4258, LMC) and to the supporting Cepheid host M31, the zeropoint  $zp$  of the Cepheid P-L relation in the LMC ground observations, the Hubble parameter and the dummy parameter mentioned above (tightly constrained to 0). This is a total of 47 parameters (46 if the dummy parameter  $X$  is ignored).

In addition to these parameters, there are other modeling parameters like the color and shape correction slopes of SnIa (usually denoted as  $\beta$  and  $\alpha$ ) as well as the Wesenheit dust extinction parameter  $R_W$  which have been incorporated in the released SnIa and Cepheid apparent magnitudes and thus can not be used as independent parameters in the analysis, in contrast to the previous data release.

The provided in R21 Cepheid Wesenheit dust corrected dereddened apparent magnitudes  $m_H^W$  are connected with the Wesenheit dust extinction parameter  $R_W$  as [124] (see also Refs. [119,120])

$$m_H^W \equiv m_H - R_W(V - I) \quad (4)$$

where  $m_H$  is the observed apparent magnitude in the near-infrared  $H$  (F160W) band,  $V$  (F555W) and  $I$  (F814W) are optical mean apparent magnitudes in the corresponding bands. The empirical parameter  $R_W$  is also called 'the reddening-free "Wesenheit" color ratio' and is different from  $R_H$  which can be derived from a dust law (e.g. the Fitzpatrick law [125]). The parameter  $R_W$  corrects for both dust and intrinsic variations applied to observed blackbody colors  $V - I$ .

The provided in R21 SnIa apparent magnitudes  $m_B^0$ , standardized using light curve color  $c$  and shape  $x_1$  corrections are defined as

$$m_B^0 \equiv m_B - \alpha x_1 - \beta c = \mu + M_B \quad (5)$$

<sup>2</sup> A differential distance measurement of the SMC with respect to the LMC is used and thus LMC+SMC are considered in a unified manner in the released data.

<sup>3</sup> 45 Cepheids in N1365 are mentioned in R21 but there are 46 in the fits files of the released dataset at Github repository: [PantheonPlusSH0ES/DataRelease](https://github.com/PantheonPlusSH0ES/DataRelease).

<sup>4</sup> A total of 3130 Cepheids have been released in the data fits files but 3129 are mentioned in R21 (see Table 2). These data are also shown concisely in Table E.1 of Appendix E and may be download in electronic form.

<sup>5</sup> This parameter is not defined in R21 but is included in the data release fits files. We thank A. Riess for clarifying this point.

where  $m_B$  is the peak apparent magnitude,  $\mu$  is the SnIa distance modulus while the B-band absolute magnitude,  $M_B$ , and correction coefficients  $\alpha$  and  $\beta$  are fit directly using the SnIa data. The latest SH0ES data release provides the measured values of  $m_H^W$  and  $m_B^0$  for Cepheid and SnIa respectively which are also used in the corresponding analysis while the parameters  $R_W$ ,  $\alpha$  and  $\beta$  are fit previously and independently by the SH0ES team to provide the values of  $m_H^W$  and  $m_B^0$ .

### 1.3. The prospect of new degrees of freedom in the SH0ES data analysis

The homogeneity of the SH0ES data with respect to the parameters  $R_W$ ,  $\alpha$  and  $\beta$  has been analysed in previous studies with some interesting results. In particular, using the data of the previous SH0ES data release [119–121], it was shown [112] (see also [101] for a relevant study) that if the parameter  $R_W$  is allowed to vary among Cepheid and SnIa hosts then the fit quality is significantly improved and the best fit value of  $H_0$  is lowered to a level consistent with the inverse distance ladder best fit. In addition, a more recent analysis has allowed the parameter  $\beta$  to have a different value in Hubble flow SnIa ( $\beta = \beta_{HF}$  for  $z > 0.02$ ) compared to calibrating SnIa ( $\beta = \beta_{cal}$  for  $z < 0.01$ ). A reanalysis allowing for this new degree of freedom has indicated a tension between the two best fit values ( $\beta_{HF}$  and  $\beta_{cal}$ ) at a level of up to  $3.8\sigma$  [105].

Motivated by these hints for inhomogeneities in the SH0ES data, in what follows we introduce new degrees of freedom in the analysis that are designed to probe the origin of these inhomogeneities. We thus accept three of the four above mentioned assumptions that have lead to the Hubble tension and test the validity of the fourth assumption. In particular we keep the following assumptions:

1. There are no significant systematics in the SH0ES data and thus they are reliable.
2. The CMB sound horizon scale used as a calibrator in the inverse distance ladder approach is correctly obtained in the standard model using the known particles.
3. The Hubble expansion history from the time of recombination up to  $z = 0.01$  (or even  $z = 0$ ) used in the inverse distance ladder measurement of  $H_0$  is provided correctly by the standard Planck18/ΛCDM cosmological model.

As discussed above there are several studies in the literature that support the validity of these assumptions (e.g. [40,92]). If these assumptions are valid then the most probable source of the Hubble tension is the violation of the fourth assumption stated above namely '*the physical laws involved and the calibration properties of Cepheids and SnIa in all the rungs of the distance ladder are well understood and modelled properly*'.

If this assumption is violated then the modeling of Cepheids+SnIa should be modified to take into account possible changes of physics by introducing new degrees of freedom that were suppressed in the original (baseline) SH0ES analysis. In the context of this approach, if these degrees of freedom are properly introduced in the analysis then the best fit value of  $H_0$  will become consistent with the corresponding inverse distance ladder value of  $H_0 = 67.36 \pm 0.54 \text{ km s}^{-1} \text{ Mpc}^{-1}$ .

In an effort to pursue this approach for the resolution of the Hubble tension we address the following questions:

- How can new degrees of freedom (new parameters) be included in the SH0ES data analysis for the determination of  $H_0$ ?
- What are the new degrees of freedom that can expose internal tensions and inhomogeneities in the Cepheid/SnIa data?
- What new degrees of freedom can lead to a best fit value of  $H_0$  that is consistent with Planck?

The main goal of the present analysis is to address these questions. The new degree of freedom we allow and investigate is a transition of any one of the four Cepheid/SnIa modeling

parameters at a specific distance  $D_c$  or equivalently (in the context of the cosmological principle) at a given cosmic time  $t_c$  such that  $t_0 - t_c = D_c/c$  where  $t_0$  is the present cosmic time (age of the Universe). In the context of this new degree of freedom we reanalyse the SH0ES data to find how does the quality of fit to the data and the best fit value of  $H_0$  change when the new degree of freedom is excited. The possible introduction of new constraints included in the analysis is also considered.

The structure of this paper is the following: In the next section 2 we describe the standard analysis of the SH0ES Cepheid+SnIa data in a detailed and comprehensive manner stressing some details of the released dataset that are not described in R21. We also describe some tension between the values of the best fit Cepheid modeling parameters  $b_W$  and  $Z_W$  obtained in anchor or pure Cepheid host galaxies and the corresponding mean values obtained in SnIa host galaxies. In section 3 we present our generalized analysis with new degrees of freedom that allow a transition of the main modeling parameters at specific distances (cosmic times of radiation emission). We also investigate the effect of the inverse distance ladder constraint on  $M_B$  [115,126,127] for both the baseline SH0ES analysis and for our analysis involving the  $M_B$  transition degree of freedom. Finally in section 4 we conclude, discuss the implications of our results and the possible extensions of our analysis.

## 2. The new SH0ES data and their standard analysis: Hints for intrinsic tensions

### 2.1. The original baseline SH0ES analysis: a comprehensive presentation

The main equations used to model the Cepheid SnIa measured apparent magnitudes with parameters that include  $H_0$  are described as follows:

- The equation that connects the measured Wesenheit magnitude of the  $j$ th Cepheid in the  $i$ th galaxy, with the host distance moduli  $\mu_i$  and the modeling parameters  $M_W$ ,  $b_W$  and  $Z_W$  is of the form<sup>6</sup>

$$m_{H,i,j}^W = \mu_i + M_{H,i}^W + b_W[P]_{i,j} + Z_W[O/H]_{i,j} \quad (6)$$

where  $\mu_i$  is the inferred distance modulus to the galaxy,  $M_H^W$  is the zeropoint Cepheid absolute magnitude of a period  $P = 10 d$  Cepheid ( $d$  for days), and  $b_W$ - $Z_W$  are the slope parameters that represent the dependence of magnitude on both period and metallicity. The  $[O/H]$  is a measure of the metallicity of the Cepheid. The usual bracket shorthand notation for the metallicity  $[O/H]$  represents the Cepheid metal abundance compared to that of the Sun

$$[O/H] \equiv \log(O/H) - \log(O/H)_\odot = \Delta \log(O/H) \quad (7)$$

Here O and H is the number of oxygen and hydrogen atoms per unit of volume respectively. The unit often used for metallicity is the dex (decimal exponent) defined as  $n \text{ dex} \equiv 10^n$ . Also, the bracket shorthand notation for the period  $[P]$  is used as ( $P$  in units of days)

$$[P] \equiv \log P - 1 \quad (8)$$

- The color and shape corrected SnIa B-band peak magnitude in the  $i$ th host is connected with the distance modulus  $\mu_i$  of the  $i$ th host and with the SnIa absolute magnitude  $M_B$  as shown in Eq. (5) i.e.

$$m_{B,i}^0 = \mu_i + M_B \quad (9)$$

<sup>6</sup> For Cepheids in the LMC/SMC anchor observed from the ground the zeropoint parameter  $zp$  is added on the RHS and thus Eq. (6) becomes  $m_{H,i,j}^W = \mu_i + M_{H,i}^W + b_W[P]_{i,j} + Z_W[O/H]_{i,j} + zp$  to allow for a different P-L zeropoint between ground and HST observations.

The distance modulus is connected with the luminosity distance  $d_L$  in  $Mpc$  as

$$\mu = 5 \log(d_L/Mpc) + 25 \quad (10)$$

where in a flat universe

$$d_L(z) = c(1+z) \int_0^z \frac{dz'}{H(z')} = cH_0^{-1}(1+z) \int_0^z \frac{H_0}{H(z')} dz' \equiv H_0^{-1} D_L(z) \quad (11)$$

where  $D_L(z)$  is the Hubble free luminosity distance which is independent of  $H_0$ .

- Using Eqs. (9)-(11) it is easy to show that that  $H_0$  is connected with the SnIa absolute magnitude and the Hubble free luminosity distance as

$$5 \log H_0 = M_B + 5 \log D_L(z) - m_B^0(z) + 25 \quad (12)$$

In the context of a cosmographic expansion of  $H(z)$  valid for  $z \ll 1$  we have

$$\log D_L(z)_c \simeq \log \left[ cz \left( 1 + \frac{1}{2}(1-q_0)z - \frac{1}{6}(1-q_0-3q_0^2+j_0)z^2 + \mathcal{O}(z^3) \right) \right] \quad (13)$$

where  $q_0 \equiv -\frac{1}{H_0^2} \frac{d^2 a(t)}{dt^2} \Big|_{t=t_0}$  and  $j_0 \equiv \frac{1}{H_0^3} \frac{d^3 a(t)}{dt^3} \Big|_{t=t_0}$  are the deceleration and jerk parameters respectively. Thus Eqs. (12) and (13) lead to the equation that connects  $H_0$  with the SnIa absolute magnitude  $M_B$  which may be expressed as

$$5 \log H_0 = M_B + 5 \log D_L(z) - m_B^0(z) + 25 \equiv M_B + 5 a_B + 25 \quad (14)$$

where we have introduced the parameter  $a_B \equiv \log D_L(z) - 0.2m_B^0(z)$  as defined in the SH0ES analysis [119].

Thus the basic modeling equations used in the SH0ES analysis for the measurement of  $H_0$  are Eqs. (6), (9) and (14). In these equations the input data are the measured apparent magnitudes (luminosities) of Cepheids  $m_{H,i,j}^W$  and the SnIa apparent magnitudes  $m_{B,i}^0$  (in Cepheid+SnIa hosts and in the Hubble flow). The parameters to be fit using a maximum likelihood method are the distance moduli  $\mu_i$  (of the anchors and supporting hosts, the Cepheid+SnIa hosts and Hubble flow SnIa), the four modeling parameters ( $M_H^W$ ,  $b_W$ ,  $Z_W$  and  $M_B$ ), the Hubble constant  $H_0$ , the zeropoint  $zp$  of the Cepheid P-L relation in the LMC ground measurements and the dummy parameter  $X$ . This is a total of 47 parameters. The actual data have been released by the SH0ES team as a .fits file in the form of a column vector  $Y$  with 3492 entries which includes 8 constraints on the parameters obtained from measurements in anchor galaxies where the distance moduli are measured directly with geometric methods.

The entries of the provided  $Y$  data column vector do not include the pure measured apparent magnitudes. Instead its entries are residuals defined by subtracting specific quantities. In particular:

- The Cepheid Wesenheit magnitudes are presented as residuals with respect to a fiducial P-L term as

$$\bar{m}_{H,i,j}^W \equiv m_{H,i,j}^W - b_W^0[P] \quad (15)$$

where  $b_W^0 = -3.286$  is a fiducial Cepheid P-L slope. As a result of this definition the derived best fit slope is actually a residual slope  $\Delta b_W \equiv b_W - b_W^0$ .

- The residual Cepheid Wesenheit magnitudes of the Cepheids in the anchors N4258, LMC and the supporting pure Cepheid host SMC (non SnIa hosts), are presented after subtracting a corresponding fiducial distance modulus obtained with geometric methods.<sup>7</sup>
- The SnIa standardized apparent magnitudes in the Hubble flow are presented as residuals after subtracting the Hubble free luminosity distance with cosmographic expansion  $5 \log D_L(z)_c + 25$  (see Eq. (13)).

Thus the released data vector  $\mathbf{Y}$  has the following form

$$\mathbf{Y} = \left( \begin{array}{c} \bar{m}_{H,1}^W \\ \vdots \\ \bar{m}_{H,2150}^W \\ \hline \bar{m}_{H,N4258,1}^W - \mu_{0,N4258} \\ \vdots \\ \bar{m}_{H,N4258,443}^W - \mu_{0,N4258} \\ \bar{m}_{H,M31,1}^W \\ \vdots \\ \bar{m}_{H,M31,55}^W \\ \bar{m}_{H,LMC,ground,1}^W - \mu_{0,LMC} \\ \vdots \\ \bar{m}_{H,LMC,ground,270}^W - \mu_{0,LMC} \\ \bar{m}_{H,SMC,ground,1}^W - \mu_{0,SMC} \\ \vdots \\ \bar{m}_{H,SMC,ground,143}^W - \mu_{0,SMC} \\ \bar{m}_{H,LMC,HST,1}^W - \mu_{0,LMC} \\ \vdots \\ \bar{m}_{H,LMC,HST,69}^W - \mu_{0,LMC} \\ \hline m_{B,1}^0 \\ \vdots \\ m_{B,77}^0 \\ \hline -5.803 (M_{H,HST}^W) \\ -5.903 (M_{H,Gaia}^W) \\ -0.21 (Z_{W,Gaia}) \\ 0 (X) \\ 0 (\Delta zp) \\ 0 (\Delta b_W) \\ 0 (\Delta \mu_{N4258}) \\ 0 (\Delta \mu_{LMC}) \\ \hline m_{B,1}^0 - 5 \log [cz_1(\dots)] - 25 \\ \vdots \\ m_{B,277}^0 - 5 \log [cz_{277}(\dots)] - 25 \end{array} \right) \left. \begin{array}{l} \{ 2150 \text{ Cepheids in 37 SnIa hosts} \\ \{ 980 \text{ Cepheids in non SnIa hosts} \\ \{ 77 \text{ SnIa in Cepheid hosts} \\ \{ 8 \text{ External constraints} \\ \{ 277 \text{ SnIa in Hubble flow} \end{array} \right.$$

<sup>7</sup> In the case of SMC a differential distance with respect to LMC is used.

The 8 external anchor constraints on the parameters that appear in this vector are the following:

$$\begin{aligned}
 M_H^W &= -5.803 \pm 0.082 \\
 M_H^W &= -5.903 \pm 0.025 \\
 Z_W &= -0.21 \pm 0.12 \\
 X &= 0 \pm 0.00003 \\
 \Delta zp &= 0 \pm 0.1 \\
 \Delta b_W &= 0 \pm 10 \\
 \Delta \mu_{N4258} &= 0 \pm 0.03 \\
 \Delta \mu_{LMC} &= 0 \pm 0.026
 \end{aligned} \tag{16}$$

The parameters to be fit using the  $Y$  vector data may also be expressed as a vector  $q$  with 47 entries of the following form

$$\mathbf{q} = \left( \begin{array}{c} \mu_1 \\ \dots \\ \mu_{37} \\ \Delta \mu_{N4258} \\ M_H^W \\ \Delta \mu_{LMC} \\ \mu_{M31} \\ \Delta b_W \\ M_B \\ Z_W \\ X \\ \Delta zp \\ 5 \log H_0 \end{array} \right) \quad \left. \right\} 47 \text{ parameters}$$

Using the column vectors  $Y$  and  $q$ , Eqs. (6), (9) and (14) and the constraints stated above, can be expressed in matrix multiplication form as

$$\mathbf{Y} = \mathbf{L} \mathbf{q} \tag{17}$$

with  $Y$  the matrix of measurements (data vector),  $q$  the matrix of parameters and  $L$  a model (or design) matrix which has 3492 rows corresponding to the entries of the  $Y$  data vector and 47 columns corresponding to the entries of the parameter vector  $q$ . The model matrix  $L$  also includes some data (Cepheid period and metallicity) and in the context of this baseline modeling of data has the form

$$\mathbf{L} = \left( \begin{array}{ccccccccccccc} 1 & \dots & 0 & 0 & 1 & 0 & 0 & [P]_1 & 0 & [O/H]_1 & 0 & 0 & 0 \\ \dots & \dots \\ 0 & \dots & 1 & 0 & 1 & 0 & 0 & [P]_{2150} & 0 & [O/H]_{2150} & 0 & 0 & 0 \\ \hline 0 & \dots & 0 & 1 & 1 & 0 & 0 & [P]_{N4258,1} & 0 & [O/H]_{N4258,1} & 0 & 0 & 0 \\ \dots & \dots \\ 0 & \dots & 0 & 1 & 1 & 0 & 0 & [P]_{N4258,443} & 0 & [O/H]_{N4258,443} & 0 & 0 & 0 \\ 0 & \dots & 0 & 0 & 1 & 0 & 1 & [P]_{M31,1} & 0 & [O/H]_{M31,1} & 0 & 0 & 0 \\ \dots & \dots \\ 0 & \dots & 0 & 0 & 1 & 0 & 1 & [P]_{M31,55} & 0 & [O/H]_{M31,55} & 0 & 0 & 0 \\ 0 & \dots & 0 & 0 & 1 & 1 & 0 & [P]_{LMC,ground,1} & 0 & [O/H]_{LMC,ground,1} & 0 & 1 & 0 \\ \dots & \dots \\ 0 & \dots & 0 & 0 & 1 & 1 & 0 & [P]_{LMC,ground,270} & 0 & [O/H]_{LMC,ground,270} & 0 & 1 & 0 \\ 0 & \dots & 0 & 0 & 1 & 1 & 0 & [P]_{SMC,ground,1} & 0 & [O/H]_{SMC,ground,1} & 0 & 1 & 0 \\ \dots & \dots \\ 0 & \dots & 0 & 0 & 1 & 1 & 0 & [P]_{SMC,ground,143} & 0 & [O/H]_{SMC,ground,143} & 0 & 1 & 0 \\ 0 & \dots & 0 & 0 & 1 & 1 & 0 & [P]_{LMC,HST,1} & 0 & [O/H]_{LMC,HST,1} & 0 & 0 & 0 \\ \dots & \dots \\ 0 & \dots & 0 & 0 & 1 & 1 & 0 & [P]_{LMC,HST,69} & 0 & [O/H]_{LMC,HST,69} & 0 & 0 & 0 \\ \hline 1 & \dots & 0 & 0 & 0 & 0 & 0 & 0 & 1 & 0 & 0 & 0 & 0 \\ \dots & \dots \\ 0 & \dots & 1 & 0 & 0 & 0 & 0 & 0 & 1 & 0 & 0 & 0 & 0 \\ \hline 0 & \dots & 0 & 0 & 1 & 0 & 0 & 0 & 0 & 0 & 0 & 0 & 0 \\ 0 & \dots & 0 & 0 & 1 & 0 & 0 & 0 & 0 & 0 & 0 & 0 & 0 \\ 0 & \dots & 0 & 0 & 0 & 0 & 0 & 0 & 0 & 1 & 0 & 0 & 0 \\ 0 & \dots & 0 & 0 & 0 & 0 & 0 & 0 & 0 & 0 & 0 & 1 & 0 \\ 0 & \dots & 0 & 0 & 0 & 0 & 0 & 0 & 0 & 0 & 0 & 0 & 0 \\ 0 & \dots & 0 & 0 & 0 & 0 & 0 & 1 & 0 & 0 & 0 & 0 & 0 \\ 0 & \dots & 0 & 0 & 0 & 0 & 0 & 0 & 0 & 0 & 0 & 0 & 0 \\ 0 & \dots & 0 & 1 & 0 & 0 & 0 & 0 & 0 & 0 & 0 & 0 & 0 \\ 0 & \dots & 0 & 0 & 0 & 1 & 0 & 0 & 0 & 0 & 0 & 0 & 0 \\ \hline 0 & \dots & 0 & 0 & 0 & 0 & 0 & 0 & 1 & 0 & 0 & 0 & -1 \\ \dots & \dots \\ 0 & \dots & 0 & 0 & 0 & 0 & 0 & 0 & 1 & 0 & 0 & 0 & -1 \end{array} \right) \quad \left. \begin{array}{l} \text{2150 Cepheids in 37 SnIa hosts} \\ \text{980 Cepheids in non SnIa hosts} \\ \text{77 SnIa in Cepheid hosts} \\ \text{8 External constraints} \\ \text{277 SnIa in Hubble flow} \end{array} \right\}$$

The system (17) has 3492 equations and 47 unknown parameter values. Thus it is over-determined and at best it can be used in the context of the maximum likelihood analysis to find the best fit parameter values that have maximum likelihood and thus minimum  $\chi^2$ . For the definition of  $\chi^2$  the measurement error matrix (covariance matrix)  $\mathbf{C}$  is needed and provided in the data release as square matrix with dimension  $3492 \times 3492$ <sup>8</sup>. In Appendix A we present the schematic form of the matrix  $\mathbf{C}$  which also includes the standard uncertainties of the constraints as diagonal elements. Using the covariance matrix that quantifies the data uncertainties and their correlation, the  $\chi^2$  statistic may be constructed as

$$\chi^2 = (\mathbf{Y} - \mathbf{L}\mathbf{q})^T \mathbf{C}^{-1} (\mathbf{Y} - \mathbf{L}\mathbf{q}) \quad (18)$$

The numerical minimization of  $\chi^2$  in the presence of 47 parameters that need to be fit would be very demanding computationally even with the use of Markov chain Monte Carlo (MCMC) methods. Fortunately, the linear form of the system (17) allows the analytical minimization of  $\chi^2$  and the simultaneous analytic evaluation of the uncertainty of each parameter. In Appendix B we show that the analytic minimization of  $\chi^2$  of Eq. (18) leads to the best fit parameter maximum likelihood vector

$$\mathbf{q}_{\text{best}} = (\mathbf{L}^T \mathbf{C}^{-1} \mathbf{L})^{-1} \mathbf{L}^T \mathbf{C}^{-1} \mathbf{Y} \quad (19)$$

<sup>8</sup> The  $\mathbf{Y}$ ,  $\mathbf{L}$  and  $\mathbf{C}$  matrices are publicly available as fits files by SH0ES team at Github repository: [Pantheon-PlusSH0ES/DataRelease](https://github.com/Pantheon-PlusSH0ES/DataRelease).

The  $1\sigma$  standard errors for the parameters in  $\mathbf{q}_{\text{best}}$  are obtained as the square roots of the 47 diagonal elements of the transformed error matrix

$$\Sigma = (\mathbf{L}^T \mathbf{C}^{-1} \mathbf{L})^{-1} \quad (20)$$

For example the best fit of the parameter<sup>9</sup>  $5 \log H_0$  is obtained as the 47th entry of the best fit parameter vector  $\mathbf{q}_{\text{best}}$  and the corresponding  $1\sigma$  standard error is the  $\sqrt{\Sigma_{47,47}}$  element of the error matrix. Using equations (19) and (20) and the latest released data of the SH0ES team presented in R21 we find full agreement with all values of the best fit parameters. For example for  $H_0$  we find (after implementing error propagation)  $H_0 = 73.04 \pm 1.04 \text{ km s}^{-1} \text{ Mpc}^{-1}$  fully in agreement with the published result of R21.

In Table 1 we show the best fit values and uncertainties for all 47 parameters of the vector  $\mathbf{q}$  including the four Cepheid modeling parameters ( $b_W = b_W^0 + \Delta b_W \equiv -3.286 + \Delta b_W$ ,  $M_H^W$ ,  $Z_W$  and  $M_B$ ) along with best fit value of  $H_0$  for the baseline SH0ES model. The corresponding best fit values and uncertainties with an additional constraint on  $M_B$  from the inverse distance ladder is also included and discussed in detail in the next section. The agreement with the corresponding results of R21 (left three columns) is excellent.

Before closing this subsection we review a few points that are not mentioned in R21 but are useful for the reproduction of the results and the analysis

- The number of entries of the parameter vector  $\mathbf{q}$  is 47 and not 46 as implied in Ref. R21 due to the extra dummy parameter  $X$  which is included in the released data  $\mathbf{Y}$ ,  $\mathbf{L}$  and  $\mathbf{C}$  but not mentioned in R21.
- The entry referred as  $b_W$  in R21 in the parameter vector  $\mathbf{q}$  should be  $\Delta b_W$  because it is actually the residual  $b_W$  ( $\Delta b_W \equiv b_W - b_W^0$ ) as stated above and not the original slope of the P-L relation (its best fit value is  $\Delta b_W = -0.014 \pm 0.015$ ).
- The number of constraints shown in the definition of the  $\mathbf{Y}$  vector in R21 is 5 while in the actual released data  $\mathbf{Y}$ ,  $\mathbf{L}$  and  $\mathbf{C}$  we have found the 8 constraints defined above.

## 2.2. Homogeneity of the Cepheid modeling parameters

Before generalizing the model matrix  $\mathbf{L}$  with new degrees of freedom and/or constraints, it is interesting to test the self-consistency of the assumed universal modeling parameters  $b_W$  and  $Z_W$  of the Cepheids. These parameters can be obtained separately for each one of the  $i = 1, \dots, 40$  Cepheid hosts<sup>10</sup> by fitting linear relations.

In particular, in order to obtain the best fit P-L slope  $b_{W,i}$  of the  $i$ th Cepheid host we fit the  $m_{H,i,j}^W - \log P_{i,j}$  data (where  $P_{i,j}$  is the period in units of days of the  $j$ th Cepheid in the  $i$ th host) with a linear relation of the form

$$m_{H,i,j}^W = s_i + b_{W,i} \log P_{i,j} \quad (21)$$

with parameters to be fit in each host  $s_i - b_{W,i}$  (intercept and slope). These equations may be expressed as a matrix equation of the form

$$\mathbf{Y}_i = \mathbf{A}_i \mathbf{X}_i \quad (22)$$

<sup>9</sup> We use the standard notation  $\log \equiv \log_{10}$  which is important in the error propagation to  $H_0$ .

<sup>10</sup> 37 SnIa/Cepheid hosts and 3 pure Cepheid hosts of which 2 are anchors (N4258 and LMC).

**Table 1.** Best fit parameter values in the absence and in the presence of the inverse distance ladder constraint for baseline model.

Parameter	Best fit value	$\sigma$	Best fit value <sup>a</sup>	$\sigma^a$
$\mu_{N1309}$	32.51	0.05	32.56	0.05
$\mu_{N1365}$	31.33	0.05	31.37	0.05
$\mu_{N1448}$	31.3	0.04	31.33	0.03
$\mu_{N1559}$	31.46	0.05	31.51	0.05
$\mu_{N2442}$	31.47	0.05	31.51	0.05
$\mu_{N2525}$	32.01	0.06	32.08	0.06
$\mu_{N2608}$	32.63	0.11	32.69	0.11
$\mu_{N3021}$	32.39	0.1	32.45	0.1
$\mu_{N3147}$	33.09	0.09	33.16	0.08
$\mu_{N3254}$	32.4	0.06	32.46	0.05
$\mu_{N3370}$	32.14	0.05	32.19	0.04
$\mu_{N3447}$	31.94	0.03	31.98	0.03
$\mu_{N3583}$	32.79	0.06	32.84	0.06
$\mu_{N3972}$	31.71	0.07	31.76	0.07
$\mu_{N3982}$	31.64	0.06	31.69	0.05
$\mu_{N4038}$	31.63	0.08	31.69	0.08
$\mu_{N4424}$	30.82	0.11	30.87	0.11
$\mu_{N4536}$	30.84	0.05	30.87	0.05
$\mu_{N4639}$	31.79	0.07	31.83	0.07
$\mu_{N4680}$	32.55	0.15	32.61	0.15
$\mu_{N5468}$	33.19	0.05	33.25	0.05
$\mu_{N5584}$	31.87	0.05	31.91	0.04
$\mu_{N5643}$	30.51	0.04	30.56	0.04
$\mu_{N5728}$	32.92	0.1	32.98	0.1
$\mu_{N5861}$	32.21	0.08	32.26	0.07
$\mu_{N5917}$	32.34	0.08	32.4	0.08
$\mu_{N7250}$	31.61	0.1	31.65	0.1
$\mu_{N7329}$	33.27	0.07	33.33	0.07
$\mu_{N7541}$	32.58	0.08	32.64	0.08
$\mu_{N7678}$	33.27	0.08	33.33	0.08
$\mu_{N0976}$	33.54	0.08	33.61	0.08
$\mu_{U9391}$	32.82	0.05	32.86	0.05
$\Delta\mu_{N4258}$	-0.01	0.02	0.01	0.02
$M_H^W$	-5.89	0.02	-5.92	0.02
$\Delta\mu_{LMC}$	0.01	0.02	0.03	0.02
$\mu_{M31}$	24.37	0.07	24.4	0.07
$\Delta b_W$	-0.013	0.015	-0.026	0.015
$M_B$	-19.25	0.03	-19.33	0.02
$Z_W$	-0.22	0.05	-0.22	0.05
$X$	0.	0.	0.	0.
$\Delta zp$	-0.07	0.01	-0.07	0.01
$5 \log H_0$	9.32	0.03	9.24	0.02
$H_0$	73.04	1.04	70.5	0.7

NOTE - (a) With constraint  $M_B = -19.401 \pm 0.027$  included in the data vector  $\mathbf{Y}$  and in the model matrix  $\mathbf{L}$  with included uncertainty in the extended covariance matrix  $\mathbf{C}$ .

with  $\mathbf{Y}_i$  the vector of measurements,  $\mathbf{X}_i$  the vector of parameters and  $\mathbf{A}_i$  the model (or design) matrix. These are defined as

$$\mathbf{Y}_i = \begin{pmatrix} m_{H,i,1}^W \\ m_{H,i,2}^W \\ \vdots \\ m_{H,i,N}^W \end{pmatrix}, \quad \mathbf{X}_i = \begin{pmatrix} s_i \\ b_{W,i} \end{pmatrix}, \quad \mathbf{A}_i = \begin{pmatrix} 1 & \log P_{i,1} \\ 1 & \log P_{i,2} \\ \vdots & \vdots \\ 1 & \log P_{i,N} \end{pmatrix} \quad (23)$$

The analytically (along the lines of the previous subsection and of Appendix B) obtained minimum of

$$\chi_i^2 = (\mathbf{Y}_i - \mathbf{A}_i \mathbf{X}_i)^T \mathbf{C}_i^{-1} (\mathbf{Y}_i - \mathbf{A}_i \mathbf{X}_i) \quad (24)$$

with respect to the slope  $b_{W,i}$  and intercept  $s_i$  leads to the best fit values and standard errors for these parameters. For all Cepheids we adopt the  $N \times N$  covariance matrix  $\mathbf{C}_i$  of standard errors of the magnitude measurements from R21.

Thus, the analytic minimization of  $\chi^2$  of Eq. (24) leads to the best fit parameter maximum likelihood vector

$$\mathbf{X}_{i,\text{best}} = (\mathbf{A}_i^T \mathbf{C}_i^{-1} \mathbf{A}_i)^{-1} \mathbf{A}_i^T \mathbf{C}_i^{-1} \mathbf{Y}_i \quad (25)$$

The  $1\sigma$  standard errors for  $b_{W,i}$  slope and intercept in  $\mathbf{X}_{i,\text{best}}$  are obtained as the square roots of the 2 diagonal elements of the error matrix

$$\Sigma_i = (\mathbf{A}_i^T \mathbf{C}_i^{-1} \mathbf{A}_i)^{-1} \quad (26)$$

A similar analysis was implemented for the other Cepheid modeling parameter, the metallicity slopes  $Z_{W,i}$ . In this case the linear fit considered was of the form

$$m_{H,i,j}^W = s_i + Z_{W,i} [O/H]_{i,j} \quad (27)$$

The best fit values of the slopes  $b_{W,i}$  and  $Z_{W,i}$  for each one of the 40 Cepheid hosts are shown in Figs. 1 and 2 in terms of the host distance respectively. The actual Cepheid data in each host with the best fit  $\log P_{i,j} - m_{H,i,j}^W$  and  $[O/H]_{i,j} - m_{H,i,j}^W$  straight lines are shown in Figs. C.1 and C.2 in Appendix C for each one of the 40 Cepheid hosts  $i$ . The  $b_{W,i}$  slopes shown in Fig. C.3 for each host in sequence of increasing uncertainties, is in excellent agreement with a corresponding Figure 10 shown in R21<sup>11</sup>. The corresponding numerical values of the best fit  $b_{W,i}$  and  $Z_{W,i}$  are shown in Table C.1.

Some inhomogeneities are visible in the distance distribution of both the individual Cepheid slopes in Figs. 1 and 2 as well as in Fig. C.3. For example in Figs. 1 and C.3 there is a consistent trend of most non-anchor hosts to have an absolute best fit slope  $b_W$  that is smaller than the corresponding best fit  $b_W$  of the anchor hosts (above the dotted line). Similarly, in Fig. 2 there seems to be a trend of most  $Z_{W,i}$  absolute slopes to be larger than the corresponding slope of the the Milky Way (MW) (below the dotted line).

A careful inspection of Figs. 1 and 2 indicates that the scatter is significantly larger than the standard uncertainties of the slopes. Indeed a  $\chi^2$  fit to a universal slope for  $Z_W$  of the form

$$\chi^2(Z_W) = \sum_{i=1}^N \frac{(Z_{W,i} - Z_W)^2}{\sigma_{Z_{W,i}}^2} \quad (28)$$

<sup>11</sup> As discussed in Appendix C, 2 slopes corresponding to the hosts N4038 and N1365 are slightly shifted in our analysis compared to R21 due a small disagreement in the best fit slope and a typo of R21 in transferring the correct slope to Fig. 10 while the slope corresponding to the host N4424 is missing in Fig. 10 of R21.

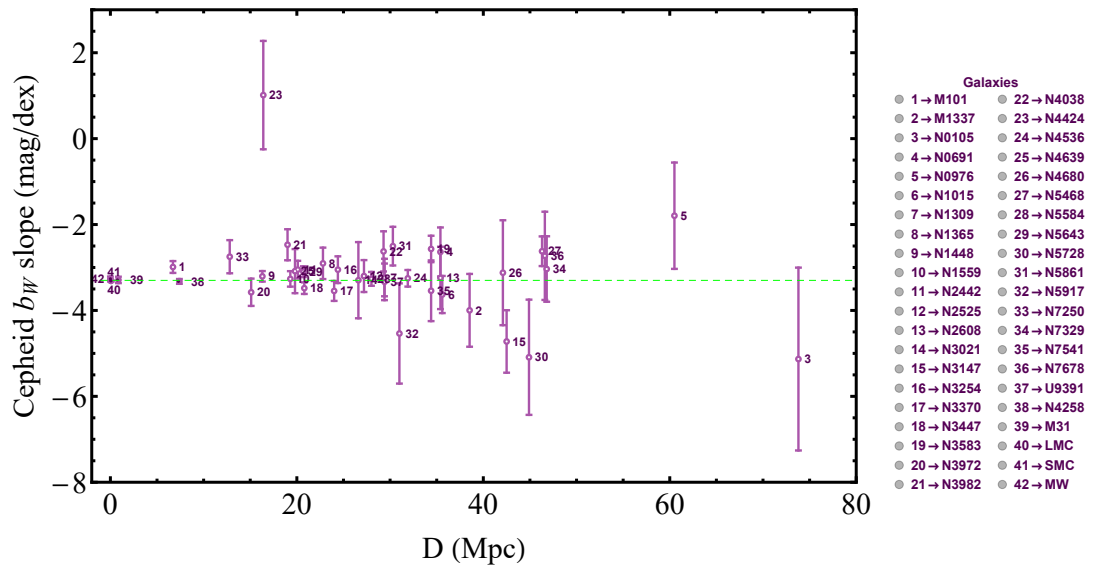


**Figure 1.** Independently fitted slopes  $b_{W,i}$  of the Cepheid P-L relations. Here we have ignored non-diagonal terms of the covariance as was done in R21 in the corresponding Figure 10. There is a consistent trend of most non-anchor hosts to have a best fit absolute slope  $|b_W|$  that is smaller than corresponding best fit  $b_W$  of the anchor hosts (above the dotted line). The dotted line corresponds to the best fit value of  $b_W = b_W^0 + \Delta b_W = -0.286 - 0.013 = -0.299$  in the context of the baseline SH0ES analysis as shown in Table 1.

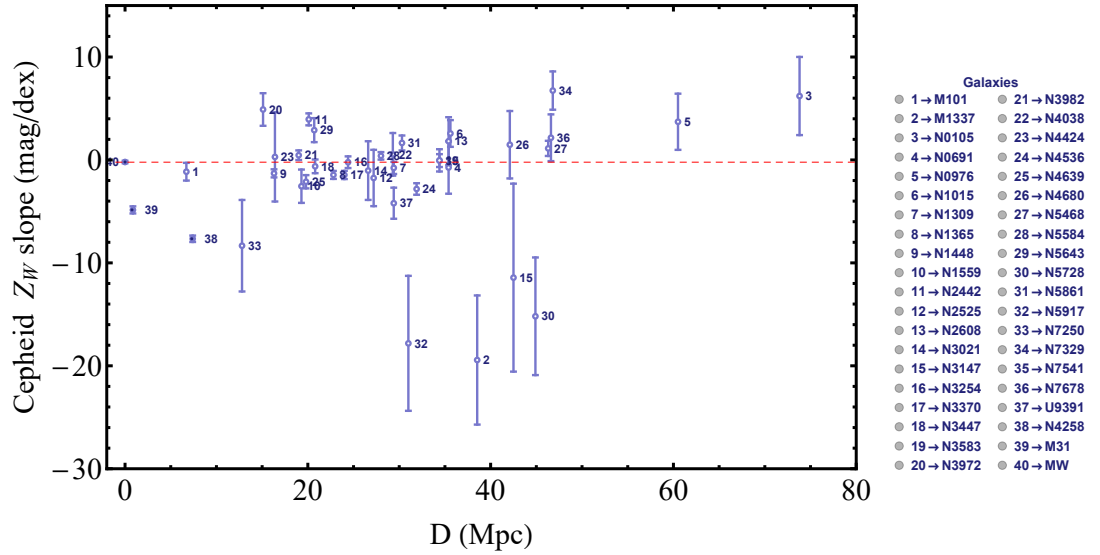


**Figure 2.** Independently fitted metallicity slopes  $Z_{W,i}$  in terms of the distance of the Cepheid host. Clearly the spread of many points is larger than the corresponding uncertainties indicating either inhomogeneities of the sample or underestimation of the uncertainties. In fact, there seems to be a trend of most  $|Z_{W,i}|$  absolute slopes to be larger than the corresponding slope of the the Milky Way (MW) (below the dotted line). The dotted line corresponds to the best fit value of  $Z_W = -0.21$  in the context of the baseline SH0ES analysis as shown in Table 1.

leads to a minimum  $\chi^2_{min}$  per degree of freedom ( $dof$ )<sup>12</sup>  $\frac{\chi^2_{ZW,min}}{dof} = 22$  (with a best fit  $Z_{W,bf} \simeq -1$ ) while  $\frac{\chi^2_{min}}{dof} = O(1)$  would be expected for an acceptable fit. Also for  $b_W$  we find  $\frac{\chi^2_{bW,min}}{dof} = 1.55$  ( $b_{W,bf} = -3.3$ ) which is more reasonable but still larger than 1 indicating a relatively poor quality of fit to a universal slope.

There are two possible causes for this poor quality of fit to universal slopes: either many of uncertainties of the individual host slopes have been underestimated or the universal slope model is not appropriate. In view of the fact that the uncertainties of the Cepheid periods and metallicities have not been included in the  $\chi^2$  fit because they were not provided by R21 released data we make the working hypothesis that the uncertainties have been underestimated and thus we add a scatter error adjusted so that  $\frac{\chi^2_{bW,min}}{dof} \simeq \frac{\chi^2_{ZW,min}}{dof} \simeq 1$ . Thus for  $\chi^2(Z_W)$  we have

$$\chi^2(Z_W) = \sum_{i=1}^N \frac{(Z_{W,i} - Z_W)^2}{\sigma_{Z_{W,i}}^2 + \sigma_{Z,scat}^2} \quad (29)$$

For  $\frac{\chi^2_{ZW,min}}{dof} \simeq 1$  we must set  $\sigma_{Z,scat} \simeq 3.2$  which is significantly larger than most uncertainties of individual host  $Z_W$  slopes. Similarly, for  $\frac{\chi^2_{bW,min}}{dof} \simeq 1$  we must set  $\sigma_{b,scat} \simeq 0.18$  which is significantly comparable or smaller than most uncertainties of individual host  $b_W$  slopes as shown in Table C.1.

In order to quantify possible inhomogeneities of Cepheid hosts  $b_{W,i}$  and  $Z_{W,i}$  slopes, we have split each sample of slopes in two bins: a low distance bin with Cepheid host distances  $D$  smaller than a critical distance  $D_c$  and a high distance bin with  $D > D_c$ . Given  $D_c$ , for each bin we find the best fit slope and its standard  $1\sigma$  error using the maximum likelihood method. For example for a low distance  $b_W$  bin we minimize

$$\chi^2(b_W^<) = \sum_{i=1}^{N^<} \frac{(b_{W,i} - b_W^<)^2}{\sigma_{b_{W,i}}^2 + \sigma_{scat}^2} \quad (30)$$

where  $N^<$  is the number of hosts in the low distance bin and  $\sigma_{scat}$  is the additional uncertainty (scatter error) chosen in each bin so that  $\chi^2 \simeq 1$  so that the fit becomes consistent with a constant  $b_W$  in each bin. Thus we find the best fit low distance bin slope  $b_W^<$  and its standard error and similarly for the high distance bin  $D > D_c$ ,  $b_W^>$  and for the slopes  $Z_W^<$ ,  $Z_W^>$ . Thus for each  $D_c$  we obtain two best fit slopes (one for each bin) and their standard errors. The level of consistency between the two binned slopes at each  $D_c$  determines the level of homogeneity and self consistency of the full sample. The results for the best fit binned slopes for  $b_W$  and  $Z_W$  are shown in Figs. 3 and 4 respectively as functions of the dividing critical distance  $D_c$ .

Interestingly, for a range of  $D_c$  there is a mild tension between the best fit values of the high and low distance bins which reaches levels of  $2 - 3\sigma$  especially for the metallicity slopes  $Z_W$ . For both  $b_W$  and  $Z_W$ , the absolute value of the difference between the high and low distance bin slopes is maximized for  $D_c > 47Mpc$ . For the case of  $Z_W$  this difference is significant statistically as it exceeds the level of  $2\sigma$ . The level of statistical consistency between high and low distance bins for both slopes  $b_W$  and  $Z_W$  is shown in Fig. 5. In the range of  $D_c$  between

<sup>12</sup> The number of degrees of freedom is  $dof = N - M = 42 - 1 = 41$  for  $b_W$  and  $dof = N - M = 40 - 1 = 39$  for  $Z_W$ . The smaller number of  $N$  for  $Z_W$  is due to the fact that metallicities were not provided for individual Cepheids in the LMC and SMS in R21 and thus we evaluated a smaller number of slopes for  $Z_W$ . See also Table C.1. The  $N = 42$  points shown in the plot 1 include the two additional points corresponding to MW and SMC (which is degenerate with LMC).

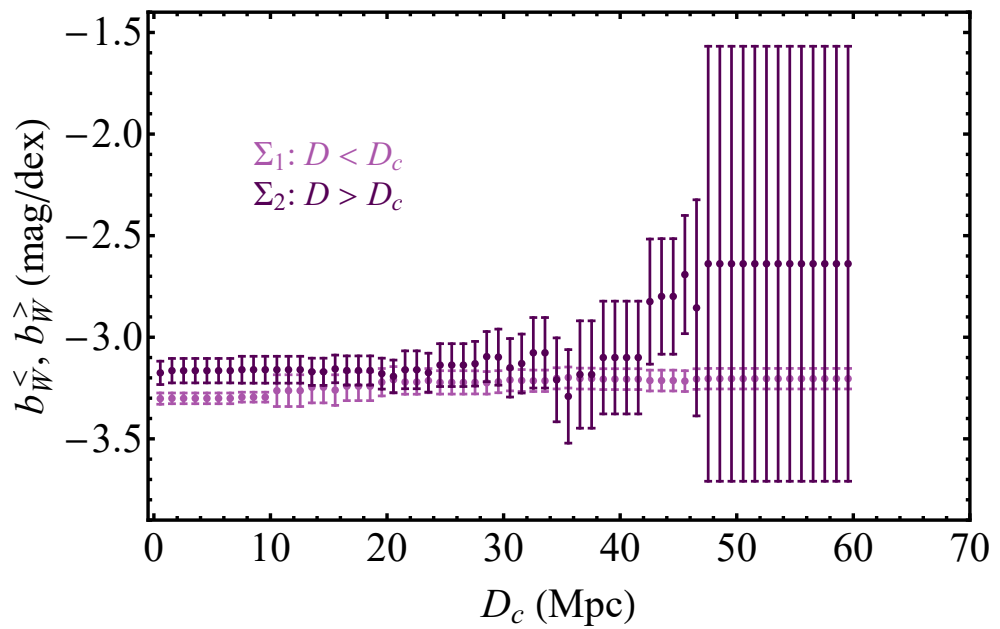


**Figure 3.** Binned Cepheid P-L slopes  $b_W^>$  and  $b_W^<$  for the high distance bin  $\Sigma_2$  ( $D > D_c$ ) and the low distance bin  $\Sigma_1$  ( $D < D_c$ ) respectively. In each bin  $\sigma_{scat}$  was used and adjusted so that  $\chi^2_{bW,min} \simeq 1$ . Notice that for  $D_c \simeq 50\,Mpc$ , the high-low distance bins are statistically consistent with each other due to small number of Cepheid in the high distance bin, but the difference of their slope best fit values is maximized.

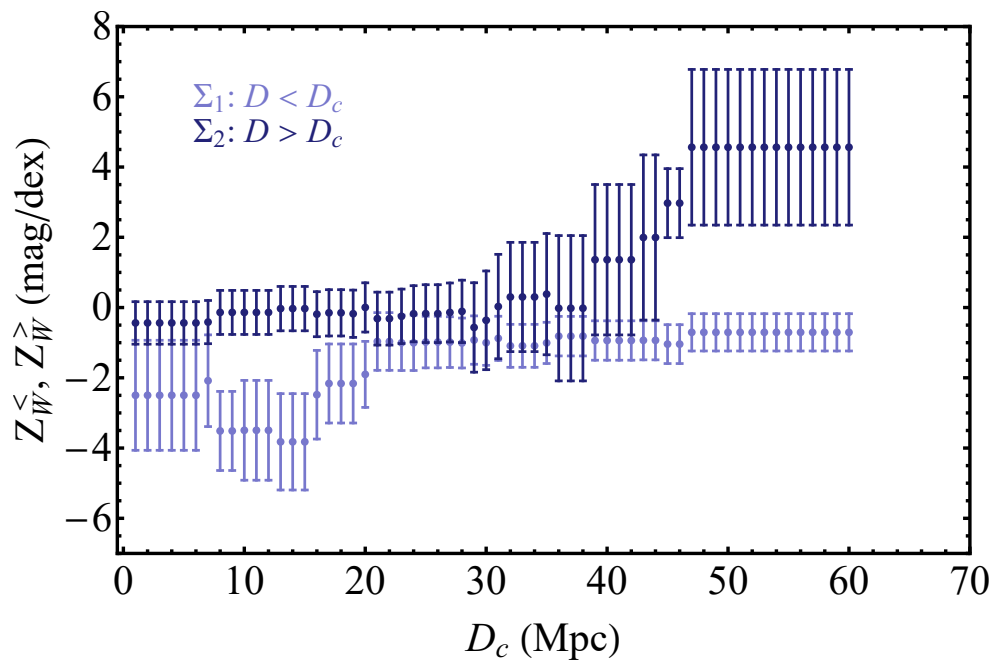


**Figure 4.** Binned Cepheid metallicity slopes  $Z_W^>$  and  $Z_W^<$  for the high distance bin  $\Sigma_2$  ( $D > D_c$ ) and the low distance bin  $\Sigma_1$  ( $D < D_c$ ) respectively. In each bin the additional scattering uncertainty  $\sigma_{scat}$  was used and adjusted so that  $\chi^2_{ZW,min} \simeq 1$ . For  $D_c \simeq 50\,Mpc$  the difference between the best fit bin slopes is maximized and the tension between them is larger than  $2\sigma$  (see also Fig. 5).

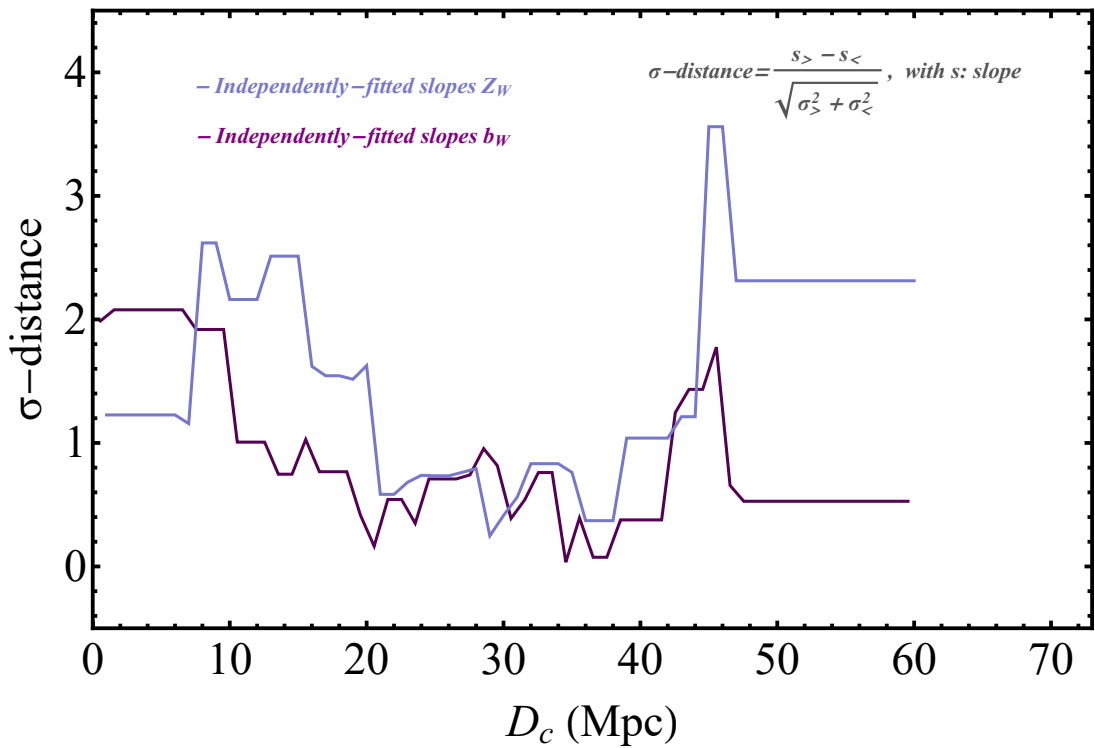


**Figure 5.** The  $\sigma$  distance between the best fit high distance bin ( $D > D_c$ ) and low distance bin slopes ( $s^>(b_W^>, Z_W^>)$  and  $s^<(b_W^<, Z_W^<)$ ) defined in Eq. (31) for  $Z_W$  and similarly for  $b_W$ .

40Mpc and 50Mpc and also between 10Mpc and 20Mpc, it is shown that in the case of  $Z_W$  the  $\sigma$ -distance

$$\sigma_d \equiv \frac{|Z_W^> - Z_W^<|}{\sqrt{\sigma_{Z_W^>}^2 + \sigma_{Z_W^<}^2}} \quad (31)$$

between the best fit binned  $Z_W$  metallicity slopes can reach a level beyond  $2\sigma$  (see Figs 4 and 5).

In view of the above identified level of mild inhomogeneities identified in the SH0ES data, it would be interesting to extend the SH0ES modeling of the Cepheids and SnIa with new degrees of freedom that can model the data taking into account these inhomogeneities. This is the goal of the next section.

### 3. Generalized analysis: New degrees of freedom allowing for a physics transition.

An obvious generalization of the SH0ES analysis described in subsection 2.1 which models the Cepheid-SnIa luminosities using four main parameters is to allow for a transition of any one of these parameters at a particular distance or equivalently cosmic time when radiation was emitted. Such a transition could be either a result of a sudden change in a physics constant (e.g. the gravitational constant) during the last 200Myrs in the context e.g. of a first order phase transition or a result of the presence of an unknown systematic.

Another modification of the standard SH0ES analysis in R21 would be to extend the number of constraints imposed on the data vector  $\mathbf{Y}$  taking into account other cosmological data like the inverse distance ladder estimate of  $M_B$  [115,126,127]. Both of these generalizations will be implemented in the present section.

### 3.1. Allowing for a transition of a Cepheid calibration parameter

A transition of one of the Cepheid calibration parameters can be implemented by replacing one of the four modeling parameters in the  $\mathbf{q}$  vector by two corresponding parameters: one for high and one for low distances (recent cosmic times). Thus, in this approach the number of parameters and entries in the parameter vector  $\mathbf{q}$  increases by one from 47 to 48. Since one of the entries of  $\mathbf{q}$  is replaced by two entries, the corresponding column of the modeling matrix  $\mathbf{L}$  should be replaced by two columns. The high distance parameter column should be similar to the original column it replaced but with zeros in entries corresponding to low distance data (or constraints) and the reverse should happen for the low distance parameter column. This process is demonstrated in the following schematic diagram where the  $q_j$  parameter is replaced by the two parameters  $q_j$  (or  $q_j^<$ ) and  $q_{j+1}$  (or  $q_j^>$ ) and the  $j$  column of  $\mathbf{L}$  is replaced by the  $j$  and  $j+1$  corresponding columns which have zeros in the low or high distance data (or constraint) entries.

$$\mathbf{L}_{(3492 \times 47)} = \left( \begin{array}{ccc} \dots & L_{1,j} & \dots \\ \dots & L_{2,j} & \dots \\ \dots & L_{3,j} & \dots \\ \dots & \dots & \dots \\ \dots & \dots & \dots \\ \dots & L_{3491,j} & \dots \\ \dots & L_{3492,j} & \dots \end{array} \right) \left\{ \begin{array}{l} D_{Y_1} < D_c \\ D_{Y_2} > D_c \\ D_{Y_3} > D_c \\ \dots \\ D_{Y_{3491}} < D_c \\ D_{Y_{3492}} > D_c \end{array} \right. \implies \mathbf{L}_{(3492 \times 48)} = \left( \begin{array}{cccc} \dots & L_{1,j} & 0 & \dots \\ \dots & 0 & L_{2,j+1} & \dots \\ \dots & 0 & L_{3,j+1} & \dots \\ \dots & \dots & \dots & \dots \\ \dots & \dots & \dots & \dots \\ \dots & L_{3491,j} & 0 & \dots \\ \dots & 0 & L_{3492,j+1} & \dots \end{array} \right) \quad (32)$$

$$\mathbf{q}_{(47 \times 1)} = \begin{pmatrix} \dots \\ \dots \\ q_j \\ \dots \\ \dots \end{pmatrix} \rightarrow \mathbf{q}_{(48 \times 1)} = \begin{pmatrix} \dots \\ \dots \\ q_j \\ q_{j+1} \\ \dots \\ \dots \end{pmatrix} \quad (33)$$

In this manner, if the parameter  $b_W$  was to be split to  $b_W^>$  and  $b_W^<$  for example, Eq. (6) would be replaced by

$$m_{H,i,j}^W(D) = \mu_i + M_{H,i}^W + b_W^> \Theta(D - D_c)[P]_{i,j} + b_W^< \Theta(D_c - D)[P]_{i,j} + Z_W[O/H]_{i,j} \quad (34)$$

and similarly for splittings of each one of the other three parameters  $M_H^W$ ,  $Z_W$  and  $M_B$ . In (34)  $D$  is a distance that may be assigned to every entry of the data-vector  $\mathbf{Y}$  (Cepheids, SNIa and constraints). Notice that the splitting of any parameter to a high and low distance version does not affect the form of the  $\mathbf{Y}$  data vector and the covariance matrix  $\mathbf{C}$  of the data. In order to properly place the 0 entries of each one of the new columns, a distance must be assigned to every entry of  $\mathbf{Y}$ . We have specified this distance for each host using the literature resources or

the best fit distance moduli of each host. These distances along with other useful properties of the Cepheids used in our analysis are shown in Table 2.

We have thus considered four generalizations of the baseline SH0ES analysis each one corresponding to a high-low distance split of each one of the four modeling parameters. For each generalization we obtained the best fit values and uncertainties of all 48 parameters of the generalized parameter vector  $\mathbf{q}$  for several values of the critical distance  $D_c \in [1, 60\text{Mpc}]$  which defined in each case the high-low distance data bins. The best fit values with uncertainties for the high-low  $D$  split parameter (green and blue points) and for  $H_0$  (red points), for each generalization considered, is shown in Figs 6, 7, 8 and 9 in terms of  $D_c$ . Dotted lines correspond to the SH0ES R21  $H_0$  best fit and to the Planck18/ΛCDM best fit for  $H_0$ . The following comments can be made on the results of Figs 6, 7, 8 and 9.

- When the SnIa absolute magnitude  $M_B$  is allowed to change at  $D_c$  ( $M_B$  transition) and for  $D_c > 47\text{Mpc}$ , the best fit value of  $H_0$  drops spontaneously to the best fit Planck18/ΛCDM value albeit with larger uncertainty  $67.33 \pm 4.65$  (see Fig. 6 and second row of Table 3). This remarkable result appears with no prior or other information from the inverse distance ladder results. Clearly, there are increased uncertainties of the best fit parameter values for this range of  $D_c$  because the most distant usable Cepheid hosts are at distances  $46.8\text{Mpc}$  (N7329),  $60.5\text{Mpc}$  (N0976) and  $73.8\text{Mpc}$  (N0105) and only two of them are at distance beyond  $47\text{Mpc}$ . These hosts (N0975 and N0105) have a total of 41 Cepheids and 4 SnIa. Due to the large uncertainties involved there is a neutral model preference for this transition degree of freedom at  $D_c > 47\text{Mpc}$  (the small drop of  $\chi^2$  by  $\Delta\chi^2 \simeq -1.5$  is balanced by the additional parameter of the model). This however changes dramatically if the inverse distance ladder constraint on  $M_B$  is included in the vector  $\mathbf{Y}$  as discussed below.
- For all four modeling parameters considered, there is a sharp increase in the absolute difference between the high-low distance best fit parameter values for  $D_c \gtrsim 47\text{Mpc}$ . The statistical significance of this split however is low due to the relatively small number of available Cepheids at  $D > 47\text{Mpc}$ .
- The best fit value of  $H_0$  changes significantly when the SnIa absolute magnitude  $M_B$  is allowed to make a transition at  $D_c > 47\text{Mpc}$  but is not significantly affected if the three Cepheid modeling parameters  $M_W$ ,  $b_W$  and  $Z_W$  are allowed to make a transition at any distance. This is probably due to the large uncertainties involved and due to the fact that  $H_0$  is only indirectly connected with the three Cepheid modeling parameters.
- Each one of the transition degrees of freedom mildly reduces  $\chi^2$  thus improving the fit to the data but these transition models are not strongly preferred by model selection criteria which penalize the extra parameter implied by these models. This is demonstrated in Figs. 10, 11 which show the values of  $\Delta\chi^2_{min}$ ,  $\Delta AIC$  and  $\Delta BIC$  of the four transition models with respect to the baseline SH0ES model for various  $D_c$  transition distances. As discussed below this changes dramatically if the inverse distance ladder constraint on  $M_B$  is introduced in the analysis.

### 3.2. The effect of the inverse distance ladder constraint

In view of the spontaneous transition of the SnIa absolute magnitude  $M_B$  that appears to lead to a Hubble tension resolution, while being mildly favored by the SH0ES data ( $\Delta\chi^2 \simeq -1.5$ ) without any inverse distance ladder information included in the fit, the following question arises:

*How does the level of preference for the  $M_B$  transition model (compared to the SH0ES baseline model) change if an additional constraint is included in the analysis obtained from the inverse distance ladder best fit for  $M_B$ ?*

**Table 2.** Properties of the Cepheid hosts considered in the analysis.

Galaxy	SnIa	Ranking in Fig. C.3	Ranking in Table 3 in R21	Ranking in Data Vector Y	$D^a$ [Mpc]	Number of fitted Cepheids	Initial point in Vector Y	Final point in Vector Y
M101	2011fe	8	1	1	6,71	259	1	259
M1337	2006D	34	2	2	38,53	15	260	274
N0691	2005W	28	4	3	35,4	28	275	302
N1015	2009ig	24	6	4	35,6	18	303	320
N0105	2007A	42	3	5	73,8	8	321	328
N1309	2002fk	25	7	6	29,4	53	329	381
N1365	2012fr	20	8	7	22,8	46	382	427
N1448	2001el,2021pit	7	9	8	16,3	73	428	500
N1559	2005df	11	10	9	19,3	110	501	610
N2442	2015F	13	11	10	20,1	177	611	787
N2525	2018gv	21	12	11	27,2	73	788	860
N2608	2001bg	31	13	12	35,4	22	861	882
N3021	1995al	35	14	13	26,6	16	883	898
N3147	1997bq,2008fv,2021hpr	32	15	14	42,5	27	899	925
N3254	2019np	16	16	15	24,4	48	926	973
N3370	1994ae	14	17	16	24	73	974	1046
N3447	2012ht	9	18	17	20,8	101	1047	1147
N3583	2015so	15	19	18	34,4	54	1148	1201
N3972	2011by	17	20	19	15,1	52	1202	1253
N3982	1998aq	19	21	20	19	27	1254	1280
N4038	2007sr	29	22	21	29,3	29	1281	1309
N4424	2012cg	40	23	22	16,4	9	1310	1318
N4536	1981B	12	24	23	31,9	40	1319	1358
N4639	1990N	27	25	24	19,8	30	1359	1388
N4680	1997bp	38	26	25	42,1	11	1389	1399
N5468	1999cp,2002cr	18	27	26	46,3	93	1400	1492
N5584	2007af	10	28	27	28	165	1493	1657
N5643	2013aa,2017cbv	6	29	28	20,7	251	1658	1908
N5728	2009Y	41	30	29	44,9	20	1909	1928
N5861	2017erp	26	31	30	30,3	41	1929	1969
N5917	2005cf	37	32	31	31	14	1970	1983
N7250	2013dy	22	33	32	12,8	21	1984	2004
N7329	2006bh	33	34	33	46,8	31	2005	2035
N7541	1998dh	30	35	34	34,4	33	2036	2068
N7678	2002dp	36	36	35	46,6	16	2069	2084
N0976	1999dq	39	5	36	60,5	33	2085	2117
U9391	2003du	23	37	37	29,4	33	2118	2150
Total					2150	1	2150	
N4258	Anchor	4	38	38	7,4	443	2151	2593
M31	Supporting	5	39	39	0,86	55	2594	2648
LMC <sup>b</sup>	Anchor	2	40	40	0,05	270	2649	2918
SMC <sup>b</sup>	Supporting	3	41	41	0,06	143	2919	3061
LMC <sup>c</sup>	Anchor	2	40	42	0,05	69	3062	3130
Total					980	2151	3130	
Total All					3130	1	3130	

NOTE - (a) Distances from [NASA/IPAC Extragalactic Database](#). (b) From the ground. (c) From HST.

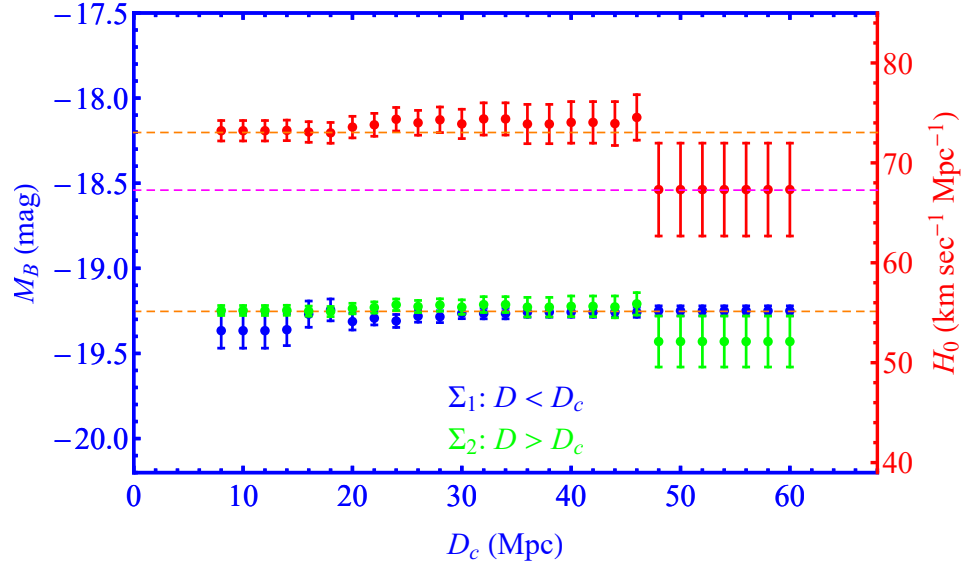


**Figure 6.** The best fit values with uncertainties for the high-low  $D$  bin of SnIa absolute magnitude  $M_B$  (green and blue points) and for  $H_0$  (red points). This generalization of the SH0ES baseline analysis allows for a transition of  $M_B$ . The best fit parameter values as shown as functions of the critical transition  $D_c$ . Dotted lines correspond to the SH0ES R21 best fit and to the Planck18/ΛCDM best fit for  $H_0$ .

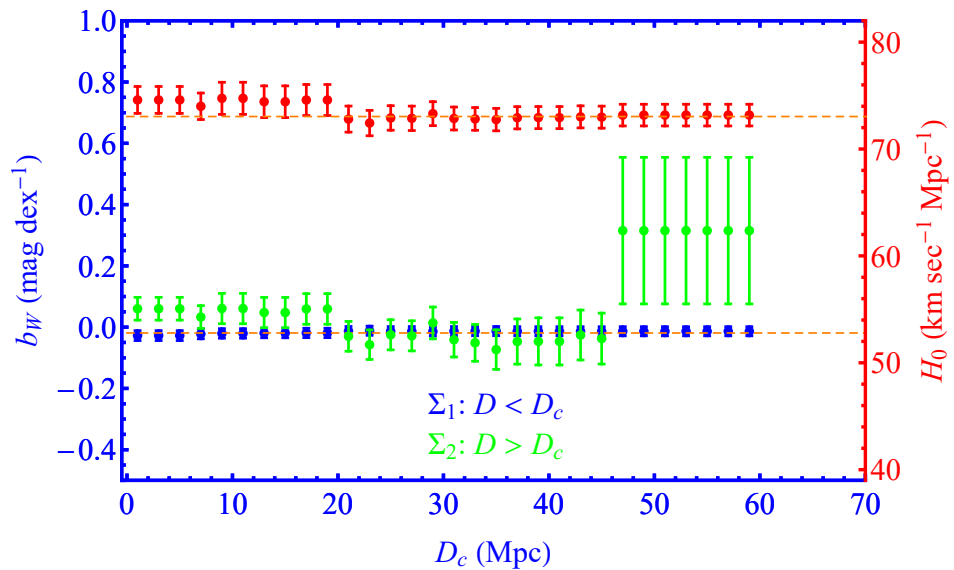


**Figure 7.** Same as Fig. 6 in an analysis generalization where the parameter  $b_W$  is allowed to have a transition at a distance  $D_c$ . Notice the sharp increase in the difference between best fit parameters high of  $D$  and low  $D$  bin  $|b_W^> - b_W^<|$  for  $D_c > 47\text{Mpc}$ .

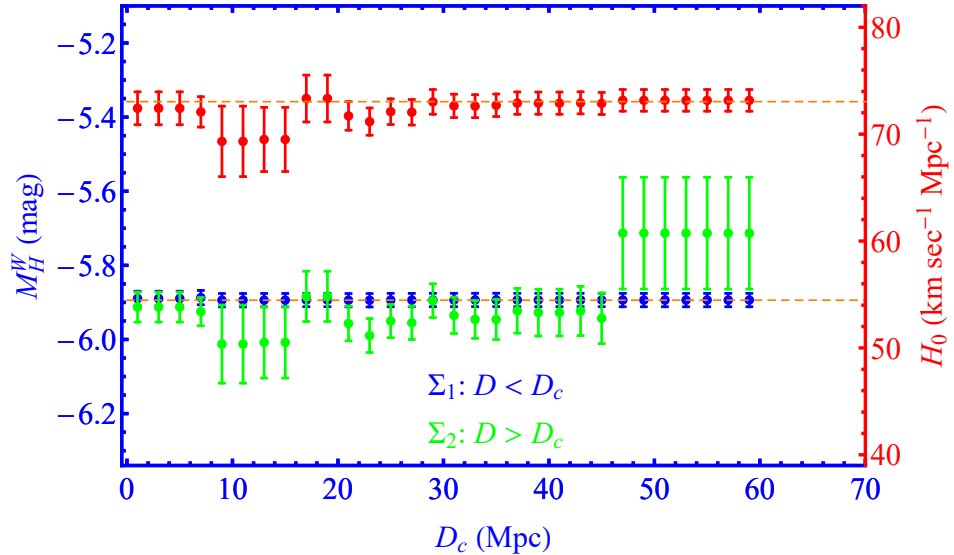


**Figure 8.** Same as Fig. 6 in an analysis generalization where the parameter  $M_W$  is allowed to have a transition at a distance  $D_c$ . Notice the sharp increase in the difference between best fit parameters of high  $D$  and low  $D$  bin  $|M_W^> - M_W^<|$  for  $D_c > 47\text{Mpc}$ .

The inverse distance ladder constraint on  $M_B$  is [115,126,127]

$$M_B^{P18} = -19.401 \pm 0.027 \quad (35)$$

In order to address this question we modify the analysis by adding one more constraint to the  $\mathbf{Y}$  data-vector: after entry 3215 which corresponds to the 8th constraint we add the value -19.401 for the  $M_B$  constraint. We also add a line to the model matrix  $\mathbf{L}$  after line 3215 with all entries set to zero except the entry at column 43 corresponding to the parameter  $M_B^<$ . A column after column 43 is added in  $\mathbf{L}$  to accommodate the high distance parameter  $M_B^>$  as described above. The new constraint is assigned a large distance (larger than the distance of the most distant SnIa of the sample) so that it only affects the high distance parameter  $M_B^>$  (the entry at line 3216 column 43 of  $\mathbf{L}$  is set to 0 for all  $D_c$  while the entry at column 44 of the same line is set to 1 for all  $D_c$ ). To accommodate the corresponding uncertainty of the new constraint we also add a line at the covariance matrix after line 3215 with a single nonzero entry at the diagonal equal to  $\sigma_{MB}^2 = 0.027^2 = 0.000729$ . Thus after the implementation of the constraint in the  $M_B$  transition model the  $\mathbf{Y}$  vector has 3493 entries, the  $\mathbf{L}$  model matrix has dimensions  $3493 \times 48$ , the  $\mathbf{q}$  parameter vector has 48 entries and the covariance matrix  $\mathbf{C}$  matrix has dimensions  $3493 \times 3493$ . In a similar way we may implement the constraint (35) in the SH0ES model without allowing for the additional transition degree of freedom and implement model selection criteria to compare the baseline with the transition model in the presence of the inverse distance ladder constraint.

The new constraints on  $H_0$  and on the parameters  $M_B^<$ ,  $M_B^>$  emerging from this modified modeling analysis are shown in Fig. 12 in terms of  $D_c$ . The corresponding quality of fit expressed via the value of  $\chi^2_{min}$  and model selection [128,129] expressed via the AIC [130] and

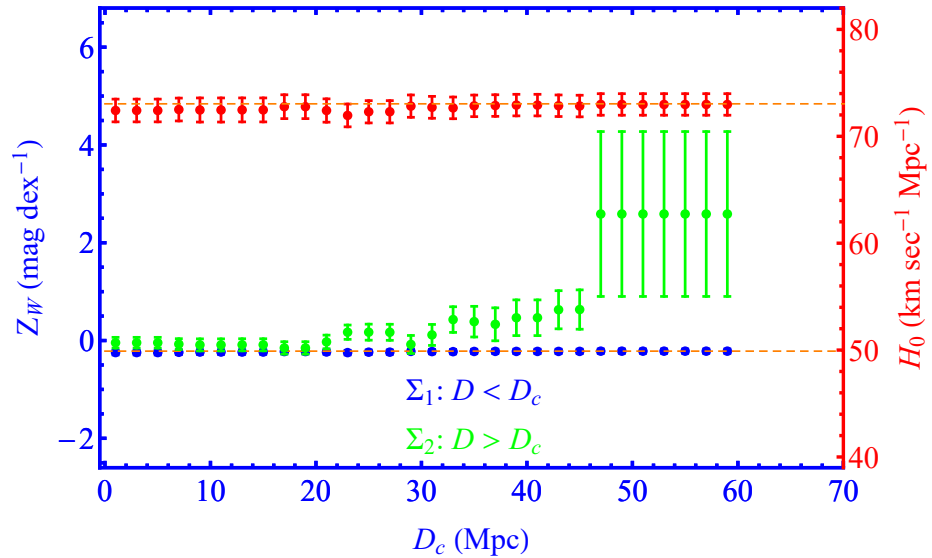


**Figure 9.** Same as Fig. 6 in an analysis generalization where the parameter  $Z_W$  is allowed to have a transition at a distance  $D_c$ . Notice the sharp increase in the difference between best fit parameters of high  $D$  and low  $D$  bin  $|Z_W^> - Z_W^<|$  for  $D_c > 47\text{Mpc}$ . The best fit value of the Hubble parameter (red points) is not significantly affected by this type of degree of freedom perhaps due to the indirect connection of  $Z_W$  with  $H_0$ .

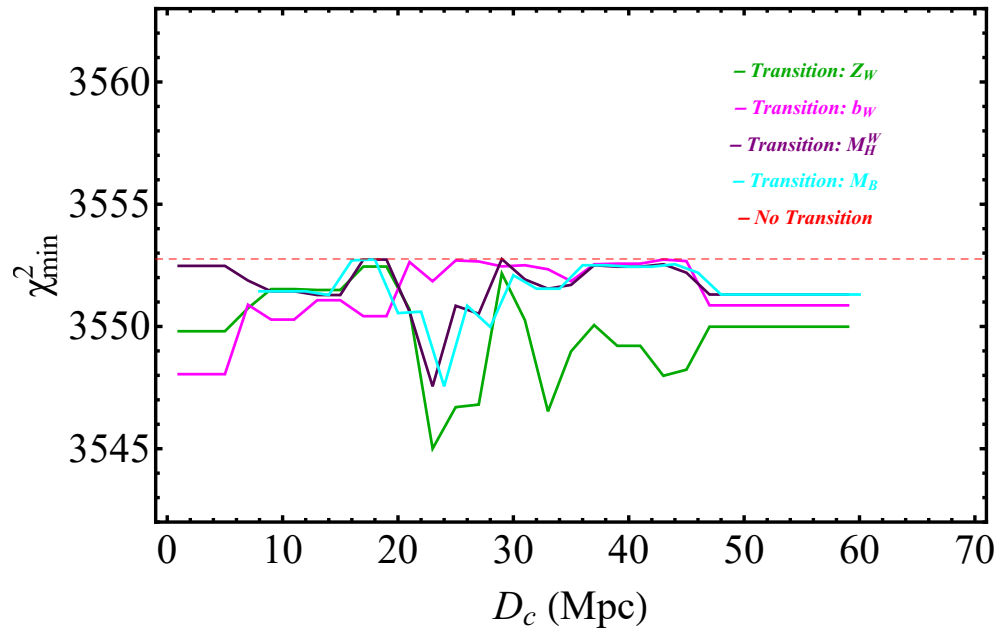


**Figure 10.** The values of  $\Delta\chi_{min}^2$  in terms of  $D_c$  for the four transition models considered with respect to the SH0ES baseline model. No inverse distance ladder constraint on  $M_B$  has been used for either the baseline or the transition models. The small improvement of the fit to the data is not enough to justify any model preference.

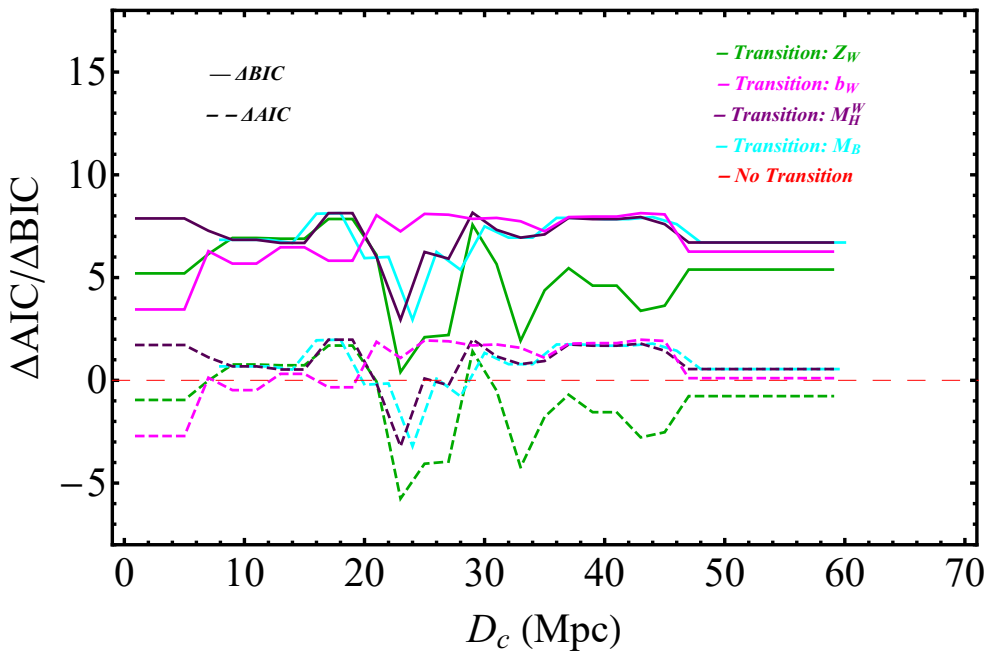


**Figure 11.** The values of  $\Delta AIC$  and  $\Delta BIC$  in terms of  $D_c$  for the four transition models considered with respect to the SH0ES baseline model. No inverse distance ladder constraint on  $M_B$  has been used for either the baseline or the transition models. The small improvement of the  $\chi^2$  fit to the data is not enough to justify any model preference. In fact the BIC which strongly penalizes any additional parameter mildly disfavors the transition models.

BIC criteria is shown in Fig. 13. The definitions and properties of the AIC and BIC criteria are described in Appendix D

Clearly, the transition degree of freedom at  $D_c \simeq 50 Mpc$  which is mildly preferred by the data even in the absence of the inverse distance ladder constraint, is strongly preferred by the data in the presence of the constraint while the  $\sigma$ -distance between the low distance best fit parameter  $M_B^<$  and the high distance  $M_B^>$  reaches a level close to  $4\sigma$ . These results are described in more detail in Table 3. The full list of the best fit values of all the parameters of the vector  $\mathbf{q}$  for the SH0ES baseline model with and without the inverse distance ladder constraint in the data vector  $\mathbf{Y}$  is shown in Table 1 along with the corresponding uncertainties.

The following comments can be made on the results shown in Table 3.

- The  $M_B$  transition degree of freedom resolves the  $H_0$  tension both in the absence of the inverse distance ladder constraint (second raw of Table 3) and in the presence of it (last row of Table 3).
- In the presence of the inverse distance ladder constraint, the model with the  $M_B$  transition degree of freedom at  $D_c = 50 Mpc$  is strongly preferred over the baseline SH0ES model as indicated by the model selection criteria despite the additional parameter it involves (comparison of the last two rows of Table 3).
- The transition degree of freedom when allowed in each one of the other three modeling parameters does not lead to a spontaneous resolution of the Hubble tension since the best fit value of  $H_0$  is not significantly affected. However, it does induce an increased absolute difference between the best fit values of the high distance and low distance parameters which however is not statistically significant due to the large uncertainties of the bin with  $D > D_c \simeq 50 Mpc$  (see also Figs. 7, 8 and 9).

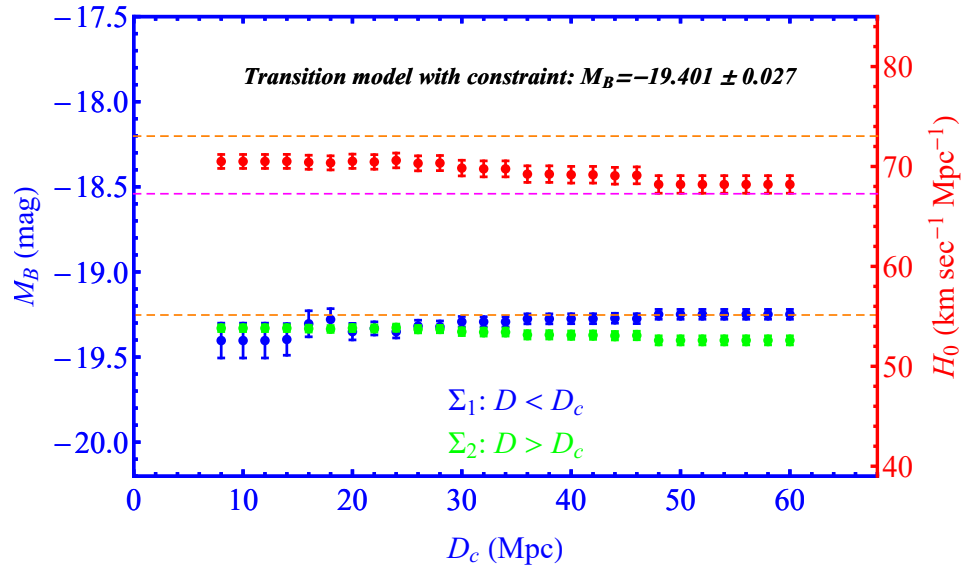


**Figure 12.** The new constraints on  $H_0$  and on the parameters  $M_B^<, M_B^>$  emerging after implementing the inverse distance ladder constraint (35) on the high distance bin of the  $M_B$  transition model.

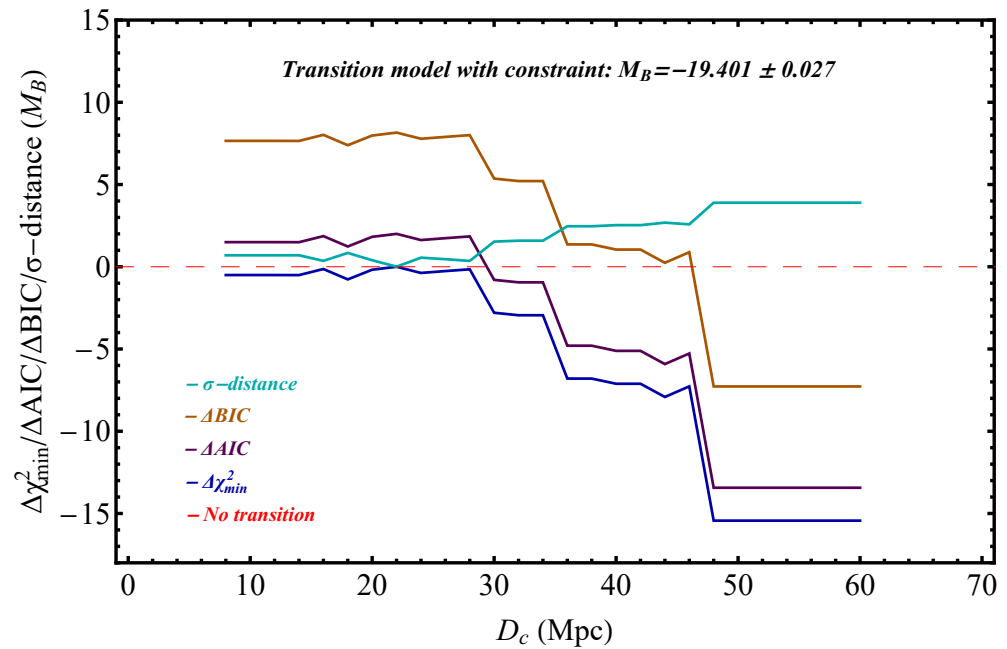


**Figure 13.** Model selection criteria of the  $M_B$  transition model with respect to the baseline SH0ES model in the presence of the inverse distance ladder constraint (35). The  $\sigma$ -distance between the low distance best fit  $M_B^<$  and the high distance  $M_B^>$  is also plotted in terms of  $D_c$ . Clearly the  $M_B$  transition model is strongly preferred with respect to the SH0ES baseline (no transition) model especially for transition distances  $D_c \simeq 50\text{Mpc}$ .

**Table 3.** A model comparison (baseline vs transitions) and best fit parameter values in the absence (top five rows) and in the presence (last two rows) of the inverse distance ladder constraint. Notice that in the presence of the inverse distance ladder constraint and the transition degree of freedom, the best fit value of  $H_0$  is identical with the inverse distance ladder result of the completed SDSS-IV extended BAO survey [30].

Model	$\chi^2_{min}$	$\chi^2_{red}^a$	$\Delta AIC$	$\Delta BIC$	$H_0$ [ $Km s^{-1} Mpc^{-1}$ ]	$M_B$ [mag]	$M_H^W$ [mag]	$\Delta b_W$ [mag/dex]	$Z_W$ [mag/dex]
Baseline	3552.76	1.031	0	0	$73.043 \pm 1.007$	$-19.253 \pm 0.029$	$-5.894 \pm 0.018$	$-0.013 \pm 0.015$	$-0.217 \pm 0.045$
Transition <sup>b</sup> $M_B$	3551.31	1.031	0.55	6.71	$67.326 \pm 4.647$	$-19.250 \pm 0.029$ $-19.430 \pm 0.150$ $1.2\sigma$	$-5.894 \pm 0.018$	$-0.013 \pm 0.015$	$-0.217 \pm 0.045$
Transition <sup>b</sup> $M_H^W$	3551.31	1.031	0.55	6.71	$73.162 \pm 1.014$	$-19.250 \pm 0.029$ $-5.713 \pm 0.151$ $1.2\sigma$	$-5.894 \pm 0.018$	$-0.013 \pm 0.015$	$-0.217 \pm 0.045$
Transition <sup>b</sup> $Z_W$	3549.99	1.030	-0.77	5.39	$72.981 \pm 1.007$	$-19.255 \pm 0.029$	$-5.894 \pm 0.018$	$-0.014 \pm 0.015$	$-0.217 \pm 0.045$ $2.588 \pm 1.686$ $1.7\sigma$
Transition <sup>b</sup> $b_W$	3550.86	1.030	0.10	6.26	$73.173 \pm 1.013$	$-19.249 \pm 0.029$	$-5.894 \pm 0.018$	$-0.013 \pm 0.015$	$-0.217 \pm 0.045$ $0.315 \pm 0.239$ $1.4\sigma$
<b>Baseline+Constraint<sup>c</sup></b>	3566.78	1.035	0	0	$70.457 \pm 0.696$	$-19.332 \pm 0.020$	$-5.920 \pm 0.017$	$-0.026 \pm 0.015$	$-0.220 \pm 0.045$
<b>Transition<sup>b,c</sup> <math>M_B+Constraint</math></b>	3551.34	1.031	-13.44	-7.27	$68.202 \pm 0.879$	$-19.249 \pm 0.029$ $-19.402 \pm 0.027$ $3.9\sigma$	$-5.893 \pm 0.018$	$-0.013 \pm 0.015$	$-0.217 \pm 0.045$

NOTE - (a)  $\chi^2_{red} = \chi^2_{min} / dof$ , where  $dof = N - M$  is typically the number of degrees of freedom (with  $N$  the number of datapoints used in the fit and  $M$  the number of free parameters) for each model. (b) At critical distance  $D_c \simeq 50 Mpc$ . (c) With constraint  $M_B = -19.401 \pm 0.027$ .

The above comments indicate that interesting physical and or systematic effects may be taking place at distances at or beyond  $50\text{Mpc}$  in the SH0ES data and therefore more and better quality Cepheid/SnIa data are needed at these distances to clarify the issue. This point is further enhanced by the recent study of Ref. [105] indicating that SnIa in the Hubble flow (at distances  $D > 90\text{Mpc}$ ) appear to have different color calibration properties than SnIa in Cepheid hosts (at distances  $D < 75\text{Mpc}$ ).

#### 4. Conclusion

We have described a general framework for the generalization of the Cepheid+SnIa modeling in the new SH0ES data. Such modeling generalization approach is motivated by the increased statistical significance of the Hubble tension and may hint towards new degrees of freedom favored by the data. Such degrees of freedom may be attributed to either new physics or to unknown systematics hidden in the data.

In the present analysis we have focused on a particular type of new modeling degree of freedom allowing for a transition of any one of the four Cepheid/SnIa modeling parameters at a distance  $D_c$ . However, our analysis can be easily extended to different degrees of freedom with physical motivation. Examples include possible modeling parameter dependence on properties other than distance (e.g. dust extinction, color and stretch calibration properties etc.). In addition other degrees of freedom that could be excited by the data could involve the modeling parameters that have been absorbed in the R21 SH0ES data like the Cepheid dust extinction parameter  $R_W$  and the color and stretch SnIa calibration parameters  $\beta$  and  $\alpha$ . These degrees of freedom may also be probed and excited by the fit to the data if allowed by the modeling [105].

We have demonstrated that our proposed transition degrees of freedom are mildly excited by the SH0ES data and in the case of the SnIa absolute magnitude  $M_B$  transition degree of freedom at  $D_c \simeq 50\text{Mpc}$ , the best fit value of  $H_0$  shifts spontaneously to a value almost identical with the Planck18/ΛCDM best fit value thus annihilating the Hubble tension. However, the high distance bin in this case involves only 41 Cepheids and 4 SnIa and therefore the best fit value of  $M_B^>$  which effectively also fixes  $H_0$  involves significant uncertainties.

In the presence of the inverse distance ladder constraint on the high distance bin parameter  $M_B^>$  of the  $M_B$  transition model and on the single  $M_B$  parameter of the SH0ES model, the uncertainties reduce dramatically. The Hubble tension is fully resolved only in the presence of the  $M_B$  transition degree of freedom at  $D_c \simeq 50\text{Mpc}$ . This transition model is also strongly selected over the baseline SH0ES model with the constraint, by both model selection criteria AIC and BIC despite the penalty imposed by AIC and especially BIC on the additional parameter involved in the new modeling. This behavior along with other recent studies [105] hints towards the need of more detailed Cepheid+SnIa calibrating data at distances  $D \gtrsim 50\text{Mpc}$  i.e. at the high end of rung 2 on the distance ladder.

Our comprehensively described generalized modeling approach opens a new direction in the understanding of the Hubble tension and may be extended by the introduction of a wide range of new degrees of freedom in the SH0ES data analysis and also by the introduction of new constraints motivated by other cosmological data. Such extensions could for example involve more distance bins in the distance dependence of the four main modeling parameters. In that case the relevant column of the modeling matrix  $\mathbf{L}$  would have to be replaced by more than two columns (one for each distance bin). Such bins could also be defined not in terms of distance but in terms of other Cepheid/SnIa properties (e.g. Cepheid metallicity or period and/or SnIa light curve color or stretch). In addition, other parameters beyond the four basic modeling parameters may be considered including the dust extinction parameter  $R_W$  and/or the SnIa light curve color and stretch parameters. Also, similar modeling generalizations may

be implemented on different distance calibrator data used for the measurement of  $H_0$  such as the TRGB data [131].

Physical motivation is an important factor for the evaluation of any new modeling degree of freedom especially if it is favored by the data. A transition of the SnIa luminosity at a particular recent cosmic time could be induced by a sudden change of the value of a fundamental physics constant e.g. the gravitational constant in the context of a recent first order phase transition [132–134] to a new vacuum of a scalar-tensor theory or in the context of a generalization of the symmetron screening mechanism [118]. A similar first order transition is implemented in early dark energy models [135] attempting to change the last scattering sound horizon scale without affecting other well constrained cosmological observables. Thus, even though no relevant detailed analysis has been performed so far, there are physical mechanisms that could potentially induce the SnIa luminosity transition degree of freedom.

The emerging new puzzles challenging our standard models may soon pave the way to exciting discoveries of new physical laws. The path to these discoveries goes through the deep and objective understanding of the true information that is hidden in the cosmological data. The present analysis may be a step in that direction.

---

**Funding:** This work was supported by the Hellenic Foundation for Research and Innovation (HFRI - Project No: 789).

**Data Availability Statement:** The numerical files for the reproduction of the figures can be found in the [A reanalysis of the SH0ES data for  \$H\_0\$](#)  GitHub repository under the MIT license.

**Acknowledgments:** We thank Adam Riess for useful comments.

**Conflicts of Interest:** The authors declare no conflict of interest.

## Appendix A. Covariance Matrix

A schematic form of the non-diagonal covariance matrix used in our analysis is shown below. The symbols  $\sigma_{tot,i}^2$  indicate the (non-diagonal in general) covariance submatrix within the  $i$  host while the symbols  $Z_{cov}$  indicate submatrices that correlate the uncertainties between different hosts.

## Appendix B. : Analytic minimization of $\chi^2$ .

The proof of Eqs. (19) and (20) that lead to the best fit parameter values and their uncertainties through the analytic minimization of  $\chi^2$  may be sketched as follows<sup>13</sup>:

Using the matrix of measurements (data vector)  $\mathbf{Y}$ , the matrix of parameters  $\mathbf{q}$  and the equation (or design) matrix  $\mathbf{L}$  with the measurement error matrix (covariance matrix)  $\mathbf{C}$  the  $\chi^2$  statistic is expressed as

$$\chi^2 = (\mathbf{Y} - \mathbf{L}\mathbf{q})^T \mathbf{C}^{-1} (\mathbf{Y} - \mathbf{L}\mathbf{q}) = \mathbf{q}^T \mathbf{L}^T \mathbf{C}^{-1} \mathbf{L}\mathbf{q} - 2\mathbf{q}^T \mathbf{L}^T \mathbf{C}^{-1} \mathbf{Y} + \mathbf{Y}^T \mathbf{C}^{-1} \mathbf{Y} \quad (\text{A1})$$

The  $\chi^2$  is minimized with respect to the parameters  $\mathbf{q}$ , by solving the equation

$$\frac{\partial \chi^2}{\partial \mathbf{q}} \Big|_{\mathbf{q}_{\text{best}}} = 0 \Rightarrow 2\mathbf{L}^T \mathbf{C}^{-1} \mathbf{L}\mathbf{q}_{\text{best}} - 2\mathbf{L}^T \mathbf{C}^{-1} \mathbf{Y} = \mathbf{0} \quad (\text{A2})$$

Thus the maximum-likelihood parameters are given as

$$\mathbf{q}_{\text{best}} = (\mathbf{L}^T \mathbf{C}^{-1} \mathbf{L})^{-1} \mathbf{L}^T \mathbf{C}^{-1} \mathbf{Y} \quad (\text{A3})$$

The standard errors squared of the parameters in  $\mathbf{q}_{\text{best}}$  are given as the diagonal elements of the transformed covariance matrix

$$\Sigma_{kl} = \sum_i \sum_j \left[ \frac{\partial \mathbf{q}_{\text{best},k}}{\partial \mathbf{Y}_i} \right] \mathbf{C}_{ij} \left[ \frac{\partial \mathbf{q}_{\text{best},l}}{\partial \mathbf{Y}_j} \right] \quad (\text{A4})$$

or

$$\Sigma = \left[ \frac{\partial \mathbf{q}_{\text{best}}}{\partial \mathbf{Y}} \right] \mathbf{C} \left[ \frac{\partial \mathbf{q}_{\text{best}}}{\partial \mathbf{Y}} \right]^T \quad (\text{A5})$$

Thus

$$\Sigma = (\mathbf{L}^T \mathbf{C}^{-1} \mathbf{L})^{-1} \mathbf{L}^T \mathbf{C}^{-1} \mathbf{C} [(\mathbf{L}^T \mathbf{C}^{-1} \mathbf{L})^{-1} \mathbf{L}^T \mathbf{C}^{-1}]^T \quad (\text{A6})$$

$$= (\mathbf{L}^T \mathbf{C}^{-1} \mathbf{L})^{-1} \mathbf{L}^T \mathbf{C}^{-1} \mathbf{C} \mathbf{C}^{-1} \mathbf{L} (\mathbf{L}^T \mathbf{C}^{-1} \mathbf{L})^{-1} \quad (\text{A7})$$

$$= (\mathbf{L}^T \mathbf{C}^{-1} \mathbf{L})^{-1} \quad (\text{A8})$$

## Appendix C. : Reanalysis of Individual Cepheid $m_H^W$ slope data.

We use the released Cepheid P-L data ( $m_H^W - \log P$ ) to find the best fit slope  $b_W$  in each one of the 40 Cepheid hosts where the 3130 Cepheid magnitudes are distributed. We thus reproduce Figs. 9 and 10 of R21. Since the released Cepheid magnitude data due not include outliers we focus on the reproduction of the black points of Fig. 10 of R21. Our motivation for this attempt includes the following:

- It is evident by inspection of Fig. 10 of R21 (see also Fig. C.3 below) that most of the better measured  $b_W$  slopes have a smaller absolute slope than the corresponding slopes obtained from anchors+MW hosts. This makes it interesting to further test the homogeneity of these measurements and their consistency with the assumption of a global value of  $b_W$  for both anchors and SnIa hosts.
- Most of the measurements that include outliers (red points of Fig. 10 of R21) tend to amplify the above mentioned effect ie they have smaller absolute slopes  $b_W$  than the slopes obtained from the anchors.

<sup>13</sup> For more details see <https://people.duke.edu/~hpgavin/SystemID/CourseNotes/linear-least-squares.pdf>

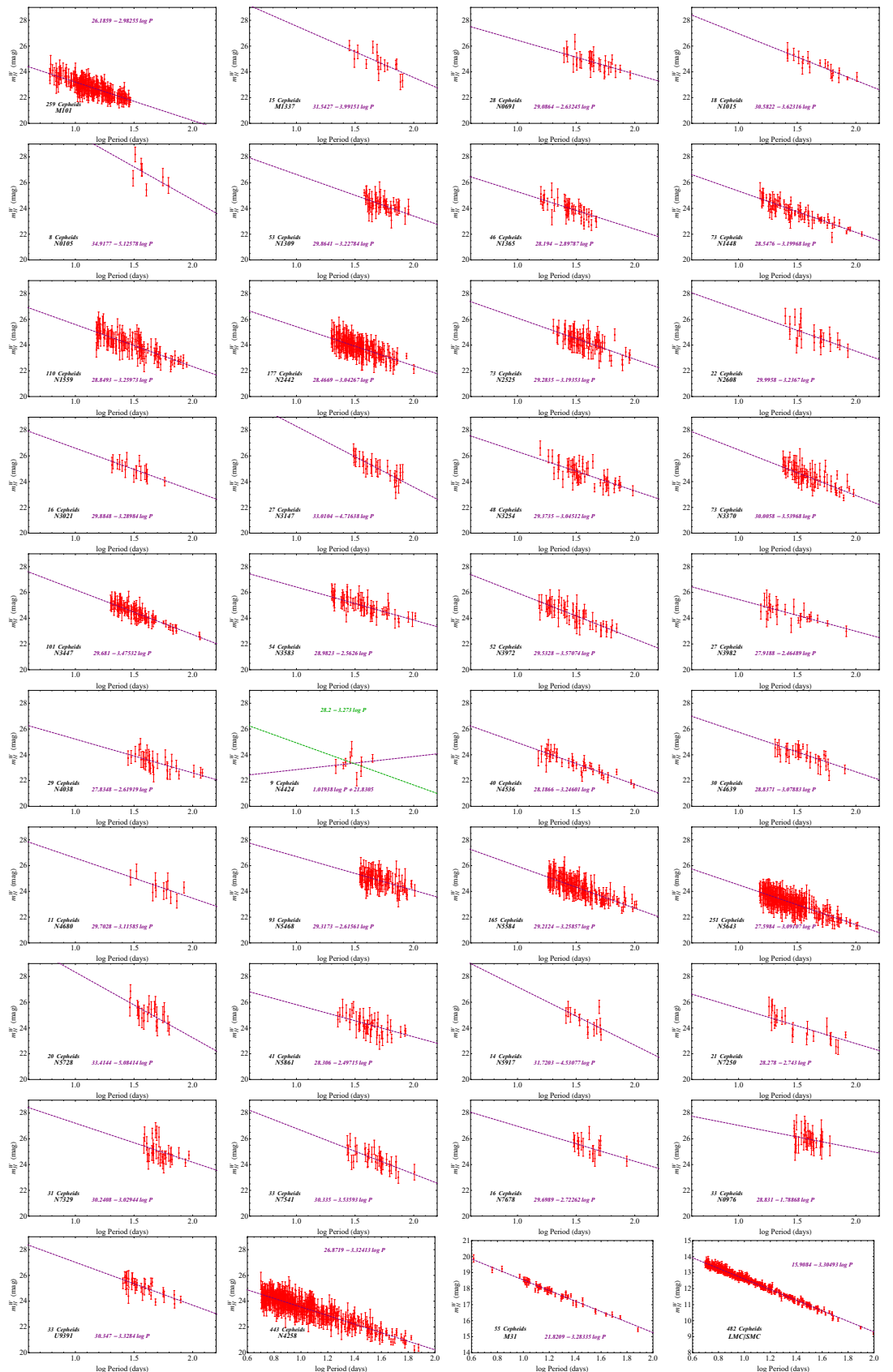


**Figure C.1.** Fitting individual slopes  $b_W$  of the  $m_H^W$  –  $\log P$ , P-L relations for 40 Cepheid hosts: 37 SnIa+Cepheid hosts, 2 anchors (N4258+LMC/SMC) and the pure Cepheid host M31. In the case of the SnIa+Cepheid host N4424 our fit (purple line) is not in agreement with the fit of R21 (green line). In all other cases the agreement is very good.

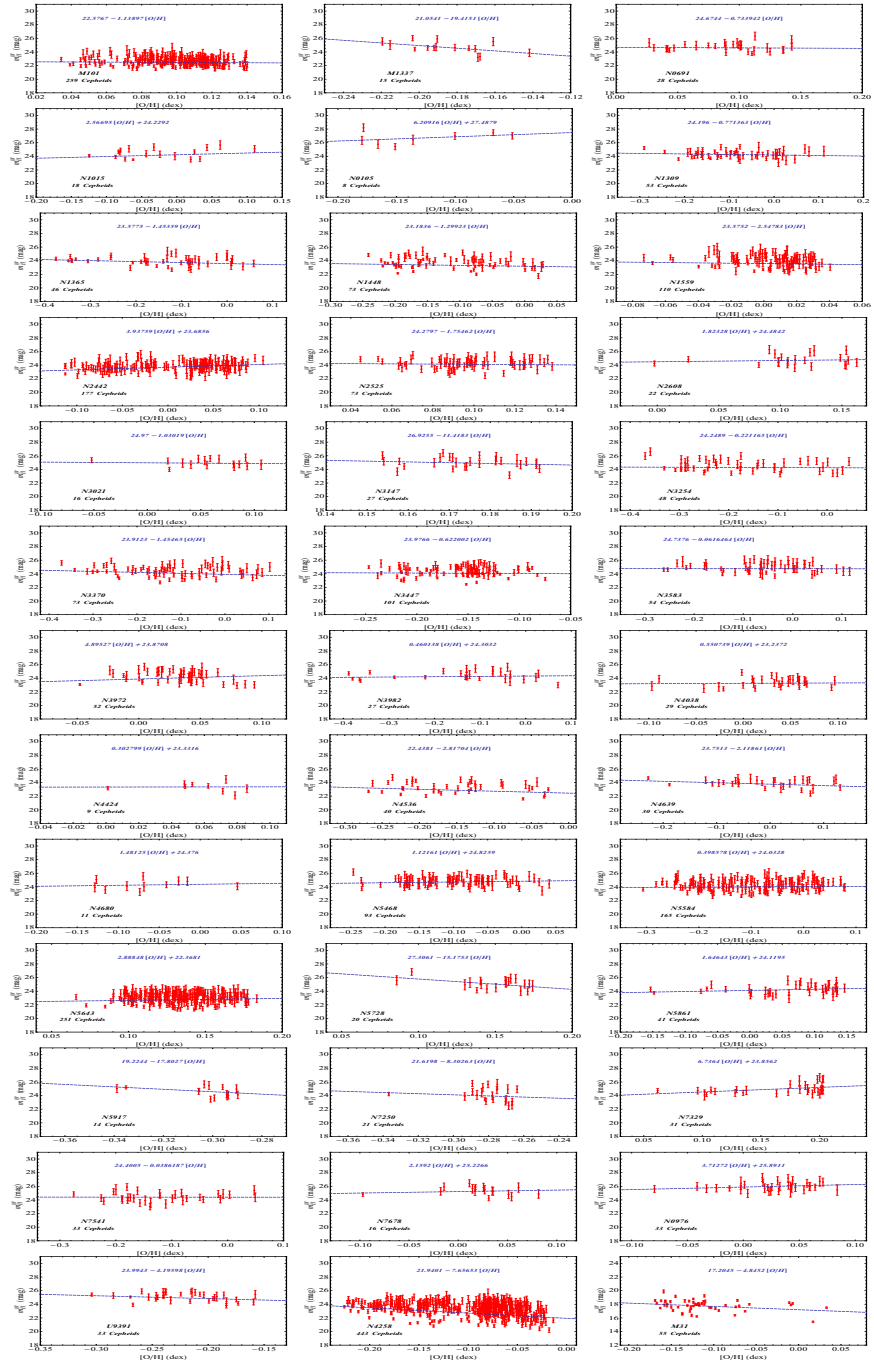


**Figure C.2.** Fitting individual slopes  $Z_W$  of the  $m_H^W$  metallicity relations to Cepheid data for the hosts where individual Cepheid metallicity data were provided by R21 (only an average metallicity was provided for LMC/SMC and thus these Cepheid hosts are not included in the plot). Thus the 39 hosts shown correspond to the 37 SnIa+Cepheid hosts, the anchor N4258 and the pure Cepheid host M31.

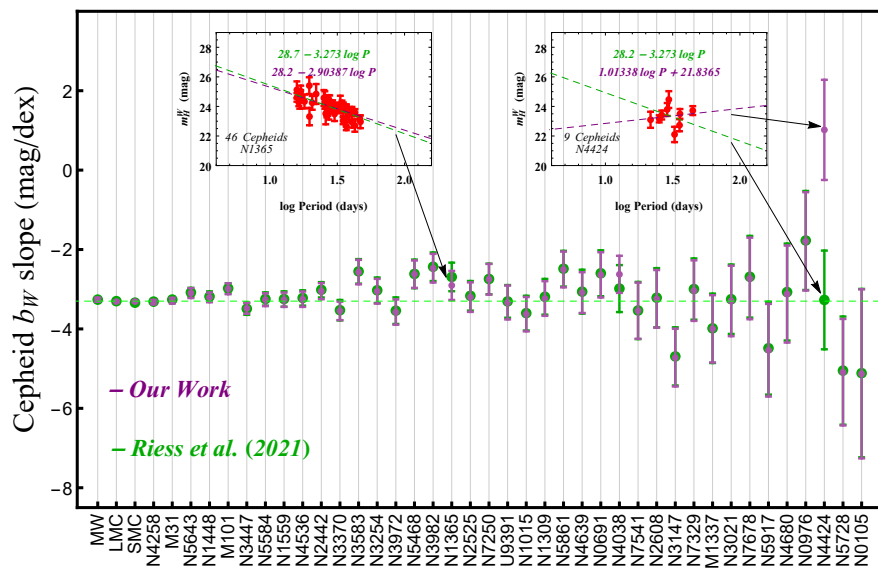


**Figure C.3.** Independently-fitted slopes  $b_W$  of the  $m_H^W$  P-L relations (without background covariance of any pair of Cepheids as was done in R21 i.e. taking into account only diagonal terms of the covariance matrix). The points in green are the corresponding points shown in Fig. 10 of R21 (obtained using plot digitizer). Our fits are in excellent agreement with R21 with the exception of 3 points corresponding to hosts N4424, N4038 and N1365. For N4424 there is no point shown in Fig. 10 of R21 but in the corresponding  $m_H^W$  –  $\log P$  plot of R21 (their Fig. 9 where the magnitudes decrease upwards on the vertical axis) the indicated best fit line is the green line shown in the upper right inset plot corresponding to the green point. The correct best fit however corresponds to the purple line of the upper right inset plot with slope given by the purple point pointed by the arrow. Similarly the best fit line corresponding to N1365 shown in the upper left inset plot is identical to our purple point and not to the green point. For the Milky Way (MW) we have used directly the values provided in R21 obtained from Gaia EDR3+HST.

- The slope corresponding to the host N4424 is missing from Fig. 10 of R21 while the host M1337 appears to show extreme behavior of the outliers.

Based on the above motivation we have recalculated all the  $b_W$  slopes of the Cepheid hosts and also extended the analysis to metallicity slopes for the Cepheids of each hosts. The individual metallicity slopes  $Z_{W,i}$  for each host have been obtained for the first time in our analysis and thus no direct comparison can be made with R21 for these slopes.

The Cepheid magnitude period and magnitude metallicity data used to calculate the corresponding best fit slopes  $b_W$  and  $Z_W$  are shown in Figs. C.1 and C.2 for each host along with the best fit straight lines from which the individual best fit  $b_{W,i}$  and  $Z_{W,i}$  were obtained. The numerical values of the derived best fit slopes along with the corresponding uncertainties are shown in Table C.1.

The derived best fit slopes  $b_{W,i}$  for each host along with their standard errors (obtained using Eqs. (25) and (26)) are shown in Fig. C.3 (purple points) along with the corresponding points of Fig. 10 of R21 (green points).

The best fit values of the slopes  $b_{W,i}$  we have obtained using the raw Cepheid data are consistent with Fig. 10 of R21 as shown in Fig. C.3. The agreement with the results of R21 is excellent except of three points. Two slopes corresponding to the hosts N4038 and N1365 are slightly shifted in our analysis compared to R21 due a small disagreement in the best fit slope and a typo of R21 in transferring the correct slope to Fig. 10.

In addition, the slope corresponding to the host N4424 is missing in Fig. 10 of R21. In the  $m_H^W - \log P$  plot of R21 (their Fig. 9 where the magnitudes decrease upwards on the vertical axis) corresponding to N4424, the indicated best fit line is the green line shown in the upper right inset plot of Fig. C.3 corresponding to the green point. The correct best fit however corresponds to the purple line of the upper right inset plot with slope given by the purple point pointed by the arrow.

Thus our Fig. C.3 is in excellent agreement with Fig. 10 of R21 with the exception of three points where our plot corrects the corresponding plot of R21. In any case we stress that these three points do not play a significant role in our conclusion about the inhomogeneities of  $b_W$  and  $Z_W$  discussed in section 2.2.

## Appendix D. Model selection criteria

Various methods for model selection have been developed and model comparison techniques used [128,129,136,137]. The reduced  $\chi^2$  is a very popular method for model comparison. This is defined by

$$\chi_{red}^2 = \frac{\chi_{min}^2}{dof} \quad (D.1)$$

where  $\chi_{min}^2$  is the minimum  $\chi^2$  and  $dof = N - M$  is typically the number of degrees of freedom (with  $N$  is the number of datapoints used in the fit and  $M$  is the number of free parameters) for each model.

The model selection methods like Akaike Information Criterion (AIC) [130] and the Bayesian Information Criterion (BIC) [138] that penalize models with additional parameters are used. For a model with  $M$  parameters and a dataset with  $N$  total observations these are defined through the relations [129,136,137]

$$AIC = -2 \ln \mathcal{L}_{max} + 2M = \chi_{min}^2 + 2M \quad (D.2)$$

$$BIC = -2 \ln \mathcal{L}_{max} + M \ln N = \chi_{min}^2 + M \ln N \quad (D.3)$$

where  $\mathcal{L}_{max} \equiv e^{-\chi_{min}^2/2}$  (e.g. [139,140]) is the maximum likelihood of the model under consideration.

**Table C.1.** The best fit individual slopes  $b_W$  and  $Z_W$  with their standard errors  $\sigma$  and scatter uncertainties  $\sigma_{scat}$ . The scatter uncertainty secures that the model of a universal best fit slope becomes an acceptable model with  $\chi^2_{min}/dof \simeq 1$ , as described in subsection 2.2. The number of hosts in the Table is  $N = 42$  including the Milky Way (MW). For LMC and SMC the metallicities were not provided individually for each Cepheid in R21 and thus no  $Z_W$  slope could be estimated in our analysis.

Galaxy	$D^a$ [Mpc]	$b_W$ [mag/dex]	$\sigma$ [mag/dex]	$\sigma_{scat}$ [mag/dex]	$Z_W$ [mag/dex]	$\sigma$ [mag/dex]	$\sigma_{scat}$ [mag/dex]
M101	6.71	-2.99	0.14	0.18	-1.14	0.86	3.2
M1337	38.53	-4.	0.85	0.18	-19.44	6.27	3.2
N0691	35.4	-2.64	0.57	0.18	-0.73	2.54	3.2
N1015	35.6	-3.63	0.43	0.18	2.57	1.3	3.2
N0105	73.8	-5.13	2.13	0.18	6.21	3.8	3.2
N1309	29.4	-3.23	0.44	0.18	-0.77	0.59	3.2
N1365	22.8	-2.9	0.37	0.18	-1.45	0.39	3.2
N1448	16.3	-3.21	0.12	0.18	-1.3	0.39	3.2
N1559	19.3	-3.27	0.18	0.18	-2.55	1.62	3.2
N2442	20.1	-3.05	0.2	0.18	3.94	0.58	3.2
N2525	27.2	-3.2	0.37	0.18	-1.75	2.74	3.2
N2608	35.4	-3.24	0.73	0.18	1.82	2.33	3.2
N3021	26.6	-3.3	0.89	0.18	-1.03	2.85	3.2
N3147	42.5	-4.72	0.73	0.18	-11.43	9.13	3.2
N3254	24.4	-3.05	0.31	0.18	-0.22	0.57	3.2
N3370	24	-3.55	0.23	0.18	-1.46	0.4	3.2
N3447	20.8	-3.48	0.13	0.18	-0.62	0.66	3.2
N3583	34.4	-2.57	0.31	0.18	-0.06	0.62	3.2
N3972	15.1	-3.58	0.32	0.18	4.9	1.58	3.2
N3982	19	-2.47	0.36	0.18	0.46	0.47	3.2
N4038	29.3	-2.63	0.47	0.18	0.54	2.07	3.2
N4424	16.4	1.01	1.26	0.18	0.29	4.33	3.2
N4536	31.9	-3.25	0.19	0.18	-2.82	0.56	3.2
N4639	19.8	-3.08	0.51	0.18	-2.12	0.64	3.2
N4680	42.1	-3.12	1.22	0.18	1.48	3.27	3.2
N5468	46.3	-2.62	0.35	0.18	1.12	0.74	3.2
N5584	28	-3.26	0.16	0.18	0.4	0.36	3.2
N5643	20.7	-3.1	0.12	0.18	2.9	1.17	3.2
N5728	44.9	-5.09	1.34	0.18	-15.19	5.71	3.2
N5861	30.3	-2.5	0.45	0.18	1.65	0.72	3.2
N5917	31	-4.54	1.17	0.18	-17.82	6.56	3.2
N7250	12.8	-2.75	0.39	0.18	-8.33	4.44	3.2
N7329	46.8	-3.04	0.76	0.18	6.74	1.86	3.2
N7541	34.4	-3.54	0.71	0.18	-0.04	1.08	3.2
N7678	46.6	-2.73	1.03	0.18	2.16	2.27	3.2
N0976	60.5	-1.79	1.24	0.18	3.71	2.73	3.2
U9391	29.4	-3.33	0.43	0.18	-4.2	1.51	3.2
N4258	7.4	-3.32	0.06	0.18	-7.67	0.31	3.2
M31	0.86	-3.29	0.07	0.18	-4.85	0.35	3.2
LMC <sup>b</sup>	0.05	-3.31	0.017	0.18	-	-	3.2
SMC <sup>b</sup>	0.06	-3.31	0.017	0.18	-	-	3.2
MW <sup>c</sup>	0	-3.26	0.05	0.18	-0.2	0.12	3.2

NOTE - (a) Distances from [NASA/IPAC Extragalactic Database](#). (b) No individual Cepheid metallicities were provided for LMC and SMC in R21 and thus we could not estimate the slope  $Z_W$  for these hosts. (c) For the Milky Way (MW) we have used directly the values provided in R21 obtained from Gaia EDR3+HST.

**Table D.1.** The interpretation of differences  $\Delta AIC$  and  $\Delta BIC$  according to the calibrated Jeffreys' scale [141] (see also Refs. [136,140,142–144]). However, it should be noted that the Jeffreys' scale has to be interpreted with care [140] because it has been shown to lead to diverse qualitative conclusions.

$\Delta AIC$			$\Delta BIC$			
Level of empirical support for the model with the smaller $AIC$				Evidence against the model with the larger $BIC$		
0-2 Substantial	4-7 Strong	> 10 Very strong	0-2 Weak	2-6 Positive	6-10 Strong	> 10 Very strong

The "preferred model" is the one which minimizes AIC and BIC. The absolute values of the AIC and BIC are not informative. Only the relative values between different competing models are relevant. Hence when comparing one model versus the baseline-SH0ES we can use the model differences  $\Delta AIC$  and  $\Delta BIC$ .

The differences  $\Delta AIC$  and  $\Delta BIC$  with respect to the baseline-SH0ES model defined as

$$\Delta AIC = AIC_i - AIC_s = \Delta\chi^2_{min} + 2\Delta M \quad (D.4)$$

$$\Delta BIC = BIC_i - BIC_s = \Delta\chi^2_{min} + \Delta M(\ln N) \quad (D.5)$$

where the subindex  $i$  refers to value of AIC (BIC) for the model  $i$  and  $AIC_s$  ( $BIC_s$ ) is the value of AIC (BIC) for the baseline-SH0ES model. Note that a positive value of  $\Delta AIC$  or  $\Delta BIC$  means a preference for baseline-SH0ES model.

According to the calibrated Jeffreys' scales [141] showed in the Table D.1 (see also Refs. [136,140,142–144]) a range  $0 < |\Delta AIC| < 2$  means that the two comparable models have about the same support from the data, a range  $4 < |\Delta AIC| < 7$  means this support is considerably less for the model with the larger  $AIC$  while for  $|\Delta AIC| > 10$  the model with the larger  $AIC$  have no support i.e. the model is practically irrelevant. Similarly, for two competing models a range  $0 < |\Delta BIC| < 2$  is regarded as weak evidence, a range  $2 < |\Delta BIC| < 6$  is regarded as positive evidence, while for  $|\Delta BIC| > 6$  the evidence is strong against the model with the larger value.

We attribute the difference between  $\Delta AIC$  and  $\Delta BIC$  for the models considered to the fact that the BIC penalizes additional parameters more strongly than the AIC as inferred by the Eqs. (D.2) and (D.3) for the used dataset with  $\ln N > 2$  (see Refs. [136,137,145]).

## Appendix E.

Here we present in a comprehensive and concise manner the 3130 Cepheid data that appear in the vector  $\mathbf{Y}$  and in the modeling matrix  $\mathbf{L}$ . The sequence is the same as the one appearing in the top 3130 entries of the vector  $\mathbf{Y}$  released in the form of fits files by R21. Even though no new information is presented in the following Table E.1 compared to the released fits files of R21, the concise presentation of these data may make them more useful in various applications and studies.

**Table E.1.** Data for 3130 Cepheids in the host SnIa host galaxies and in the anchor or supporting galaxies N4258, M31, LMC, SMC from fits files in R21. An electronic version of the complete table is available at the [A reanalysis of the SH0ES data for  \$H\_0\$](#)  GitHub repository under the MIT license.

Galaxy	Ranking in Vector Y	$\bar{m}_H^W$ [mag]	$\sigma$ [mag]	[P] [dex]	[O/H] [dex]
M1337	1	27.52	0.39	0.45	-0.2
M1337	2	28.05	0.47	0.65	-0.19
M1337	3	26.56	0.35	0.6	-0.2
M1337	4	26.97	0.27	0.78	-0.2
M1337	5	27.01	0.47	0.72	-0.18
M1337	6	26.29	0.5	0.9	-0.17
M1337	7	26.12	0.6	0.89	-0.17
M1337	8	26.94	0.45	0.75	-0.17
M1337	9	27.78	0.61	0.69	-0.16
M1337	10	26.17	0.55	0.7	-0.14
M1337	11	26.63	0.65	0.49	-0.22
M1337	12	27.4	0.39	0.85	-0.19
M1337	13	27.26	0.53	0.52	-0.22
M1337	14	27.34	0.34	0.85	-0.17
M1337	15	27	0.54	0.7	-0.19
N0691	1	26.59	0.57	0.4	0.09
N0691	2	27.1	0.46	0.61	0.06
N0691	3	26.79	0.47	0.71	0.04
N0691	4	26.83	0.5	0.78	0.14
N0691	5	26.23	0.44	0.51	0.05
N0691	6	27.16	0.48	0.63	0.1
N0691	7	26.89	0.46	0.7	0.03
N0691	8	26.75	0.59	0.43	0.03
N0691	9	27.11	0.28	0.88	0.04
N0691	10	26.99	0.68	0.62	0.1
N0691	11	27.6	0.35	0.81	0.07
N0691	12	27.33	0.38	0.75	0.08
N0691	13	26.6	0.53	0.54	0.14
N0691	14	26.34	0.45	0.74	0.09
N0691	15	26.91	0.3	0.96	0.11
N0691	16	26.79	0.49	0.84	0.13
N0691	17	27.08	0.48	0.63	0.1
N0691	18	27.07	0.59	0.63	0.1
N0691	19	26.69	0.63	0.53	0.07
N0691	20	27.94	0.58	0.49	0.11
N0691	21	26.15	0.62	0.48	0.12
N0691	22	26.46	0.43	0.74	0.11
N0691	23	27.16	0.6	0.42	0.14
N0691	24	26.96	0.38	0.8	0.14
N0691	25	26.59	0.44	0.65	0.04
N0691	26	26.61	0.52	0.5	0.09
N0691	27	26.21	0.6	0.62	0.11
N0691	28	27.42	0.65	0.65	0.1
...	...	...	...	...	...

## References

1. Riess, A.G.; et al. A Comprehensive Measurement of the Local Value of the Hubble Constant with  $1 \text{ km s}^{-1} \text{ Mpc}^{-1}$  Uncertainty from the Hubble Space Telescope and the SH0ES Team. *Astrophys. J. Lett.* **2022**, *934*, L7, [[arXiv:astro-ph.CO/2112.04510](#)]. doi:10.3847/2041-8213/ac5c5b.

2. Freedman, W.L. Measurements of the Hubble Constant: Tensions in Perspective 2021. [\[arXiv:astro-ph.CO/2106.15656\]](https://arxiv.org/abs/astro-ph.CO/2106.15656).
3. Gómez-Valent, A.; Amendola, L.  $H_0$  from cosmic chronometers and Type Ia supernovae, with Gaussian Processes and the novel Weighted Polynomial Regression method. *JCAP* **2018**, *04*, 051, [\[arXiv:astro-ph.CO/1802.01505\]](https://arxiv.org/abs/astro-ph.CO/1802.01505). doi:10.1088/1475-7516/2018/04/051.
4. Pesce, D.; et al. The Megamaser Cosmology Project. XIII. Combined Hubble constant constraints. *Astrophys. J. Lett.* **2020**, *891*, L1, [\[arXiv:astro-ph.CO/2001.09213\]](https://arxiv.org/abs/astro-ph.CO/2001.09213). doi:10.3847/2041-8213/ab75f0.
5. Freedman, W.L.; Madore, B.F.; Hoyt, T.; Jang, I.S.; Beaton, R.; Lee, M.G.; Monson, A.; Neeley, J.; Rich, J. Calibration of the Tip of the Red Giant Branch (TRGB) 2020. [\[arXiv:astro-ph.GA/2002.01550\]](https://arxiv.org/abs/astro-ph.GA/2002.01550).
6. Wong, K.C.; et al. H0LiCOW – XIII. A 2.4 per cent measurement of  $H_0$  from lensed quasars:  $5.3\sigma$  tension between early- and late-Universe probes. *Mon. Not. Roy. Astron. Soc.* **2020**, *498*, 1420–1439, [\[arXiv:astro-ph.CO/1907.04869\]](https://arxiv.org/abs/astro-ph.CO/1907.04869). doi:10.1093/mnras/stz3094.
7. Chen, G.C.F.; et al. A SHARP view of H0LiCOW:  $H_0$  from three time-delay gravitational lens systems with adaptive optics imaging. *Mon. Not. Roy. Astron. Soc.* **2019**, *490*, 1743–1773, [\[arXiv:astro-ph.CO/1907.02533\]](https://arxiv.org/abs/astro-ph.CO/1907.02533). doi:10.1093/mnras/stz2547.
8. Birrer, S.; et al. TDCOSMO - IV. Hierarchical time-delay cosmography – joint inference of the Hubble constant and galaxy density profiles. *Astron. Astrophys.* **2020**, *643*, A165, [\[arXiv:astro-ph.CO/2007.02941\]](https://arxiv.org/abs/astro-ph.CO/2007.02941). doi:10.1051/0004-6361/202038861.
9. Birrer, S.; et al. H0LiCOW - IX. Cosmographic analysis of the doubly imaged quasar SDSS 1206+4332 and a new measurement of the Hubble constant. *Mon. Not. Roy. Astron. Soc.* **2019**, *484*, 4726, [\[arXiv:astro-ph.CO/1809.01274\]](https://arxiv.org/abs/astro-ph.CO/1809.01274). doi:10.1093/mnras/stz200.
10. Fishbach, M.; et al. A Standard Siren Measurement of the Hubble Constant from GW170817 without the Electromagnetic Counterpart. *Astrophys. J. Lett.* **2019**, *871*, L13, [\[arXiv:astro-ph.CO/1807.05667\]](https://arxiv.org/abs/astro-ph.CO/1807.05667). doi:10.3847/2041-8213/aaf96e.
11. Hotokezaka, K.; Nakar, E.; Gottlieb, O.; Nissanke, S.; Masuda, K.; Hallinan, G.; Mooley, K.P.; Deller, A.T. A Hubble constant measurement from superluminal motion of the jet in GW170817. *Nature Astron.* **2019**, *3*, 940–944, [\[arXiv:astro-ph.CO/1806.10596\]](https://arxiv.org/abs/astro-ph.CO/1806.10596). doi:10.1038/s41550-019-0820-1.
12. Abbott, B.P.; et al. A gravitational-wave standard siren measurement of the Hubble constant. *Nature* **2017**, *551*, 85–88, [\[arXiv:astro-ph.CO/1710.05835\]](https://arxiv.org/abs/astro-ph.CO/1710.05835). doi:10.1038/nature24471.
13. Palmese, A.; et al. A statistical standard siren measurement of the Hubble constant from the LIGO/Virgo gravitational wave compact object merger GW190814 and Dark Energy Survey galaxies. *Astrophys. J. Lett.* **2020**, *900*, L33, [\[arXiv:astro-ph.CO/2006.14961\]](https://arxiv.org/abs/astro-ph.CO/2006.14961). doi:10.3847/2041-8213/abaeff.
14. Soares-Santos, M.; et al. First Measurement of the Hubble Constant from a Dark Standard Siren using the Dark Energy Survey Galaxies and the LIGO/Virgo Binary–Black-hole Merger GW170814. *Astrophys. J. Lett.* **2019**, *876*, L7, [\[arXiv:astro-ph.CO/1901.01540\]](https://arxiv.org/abs/astro-ph.CO/1901.01540). doi:10.3847/2041-8213/ab14f1.
15. Risaliti, G.; Lusso, E. Cosmological constraints from the Hubble diagram of quasars at high redshifts. *Nature Astron.* **2019**, *3*, 272–277, [\[arXiv:astro-ph.CO/1811.02590\]](https://arxiv.org/abs/astro-ph.CO/1811.02590). doi:10.1038/s41550-018-0657-z.
16. de Jaeger, T.; Galbany, L.; Riess, A.G.; Stahl, B.E.; Shappee, B.J.; Filippenko, A.V.; Zheng, W. A 5% measurement of the Hubble constant from Type II supernovae 2022. [\[arXiv:astro-ph.CO/2203.08974\]](https://arxiv.org/abs/astro-ph.CO/2203.08974). doi:10.1093/mnras/stac1661.
17. de Jaeger, T.; Stahl, B.; Zheng, W.; Filippenko, A.; Riess, A.; Galbany, L. A measurement of the Hubble constant from Type II supernovae 2020. [\[arXiv:astro-ph.CO/2006.03412\]](https://arxiv.org/abs/astro-ph.CO/2006.03412). doi:10.1093/mnras/staa1801.
18. Domínguez, A.; Wojtak, R.; Finke, J.; Ajello, M.; Helgason, K.; Prada, F.; Desai, A.; Paliya, V.; Marcotulli, L.; Hartmann, D. A new measurement of the Hubble constant and matter content of the Universe using extragalactic background light  $\gamma$ -ray attenuation 2019. [\[arXiv:astro-ph.CO/1903.12097\]](https://arxiv.org/abs/astro-ph.CO/1903.12097). doi:10.3847/1538-4357/ab4a0e.
19. Di Valentino, E.; Mena, O.; Pan, S.; Visinelli, L.; Yang, W.; Melchiorri, A.; Mota, D.F.; Riess, A.G.; Silk, J. In the realm of the Hubble tension—a review of solutions. *Class. Quant. Grav.* **2021**, *38*, 153001, [\[arXiv:astro-ph.CO/2103.01183\]](https://arxiv.org/abs/astro-ph.CO/2103.01183). doi:10.1088/1361-6382/ac086d.
20. Perivolaropoulos, L.; Skara, F. Challenges for  $\Lambda$ CDM: An update. *New Astron. Rev.* **2022**, *95*, [\[arXiv:astro-ph.CO/2105.05208\]](https://arxiv.org/abs/astro-ph.CO/2105.05208). doi:10.1016/j.newar.2022.101659.
21. Aghanim, N.; et al. Planck 2018 results. VI. Cosmological parameters. *Astron. Astrophys.* **2020**, *641*, A6, [\[arXiv:astro-ph.CO/1807.06209\]](https://arxiv.org/abs/astro-ph.CO/1807.06209). [Erratum: *Astron. Astrophys.* 652, C4 (2021)], doi:10.1051/0004-6361/201833910.
22. Abdalla, E.; et al. Cosmology intertwined: A review of the particle physics, astrophysics, and cosmology associated with the cosmological tensions and anomalies. *JHEAp* **2022**, *34*, 49–211, [\[arXiv:astro-ph.CO/2203.06142\]](https://arxiv.org/abs/astro-ph.CO/2203.06142). doi:10.1016/j.jheap.2022.04.002.
23. Shah, P.; Lemos, P.; Lahav, O. A buyer’s guide to the Hubble constant. *Astron. Astrophys. Rev.* **2021**, *29*, 9, [\[arXiv:astro-ph.CO/2109.01161\]](https://arxiv.org/abs/astro-ph.CO/2109.01161). doi:10.1007/s00159-021-00137-4.
24. Knox, L.; Millea, M. The Hubble Hunter’s Guide 2019. [\[arXiv:astro-ph.CO/1908.03663\]](https://arxiv.org/abs/astro-ph.CO/1908.03663).
25. Vagnozzi, S. New physics in light of the  $H_0$  tension: an alternative view. *Phys. Rev. D* **2020**, *102*, 023518, [\[arXiv:astro-ph.CO/1907.07569\]](https://arxiv.org/abs/astro-ph.CO/1907.07569). doi:10.1103/PhysRevD.102.023518.
26. Ishak, M. Testing General Relativity in Cosmology. *Living Rev. Rel.* **2019**, *22*, 1, [\[arXiv:astro-ph.CO/1806.10122\]](https://arxiv.org/abs/astro-ph.CO/1806.10122). doi:10.1007/s41114-018-0017-4.
27. Mörtsell, E.; Dhawan, S. Does the Hubble constant tension call for new physics? *JCAP* **2018**, *1809*, 025, [\[arXiv:astro-ph.CO/1801.07260\]](https://arxiv.org/abs/astro-ph.CO/1801.07260). doi:10.1088/1475-7516/2018/09/025.

28. Huterer, D.; Shafer, D.L. Dark energy two decades after: Observables, probes, consistency tests. *Rept. Prog. Phys.* **2018**, *81*, 016901, [[arXiv:astro-ph/1709.01091](https://arxiv.org/abs/astro-ph/1709.01091)]. doi:10.1088/1361-6633/aa997e.

29. Bernal, J.L.; Verde, L.; Riess, A.G. The trouble with  $H_0$ . *JCAP* **2016**, *1610*, 019, [[arXiv:astro-ph/1607.05617](https://arxiv.org/abs/astro-ph/1607.05617)]. doi:10.1088/1475-7516/2016/10/019.

30. Alam, S.; et al. Completed SDSS-IV extended Baryon Oscillation Spectroscopic Survey: Cosmological implications from two decades of spectroscopic surveys at the Apache Point Observatory. *Phys. Rev. D* **2021**, *103*, 083533, [[arXiv:astro-ph/2007.08991](https://arxiv.org/abs/astro-ph/2007.08991)]. doi:10.1103/PhysRevD.103.083533.

31. Verde, L.; Treu, T.; Riess, A.G. Tensions between the Early and the Late Universe. *Nature Astron.* **2019**, *3*, 891, [[arXiv:astro-ph/1907.10625](https://arxiv.org/abs/astro-ph/1907.10625)]. doi:10.1038/s41550-019-0902-0.

32. Schöneberg, N.; Franco Abellán, G.; Pérez Sánchez, A.; Witte, S.J.; Poulin, V.; Lesgourgues, J. The  $H_0$  Olympics: A fair ranking of proposed models **2021**. [[arXiv:astro-ph/2107.10291](https://arxiv.org/abs/astro-ph/2107.10291)].

33. Krishnan, C.; Colgáin, E.O.; Ruchika, S.; Sen, A.A.; Sheikh-Jabbari, M.M.; Yang, T. Is there an early Universe solution to Hubble tension? *Phys. Rev. D* **2020**, *102*, 103525, [[arXiv:astro-ph/2002.06044](https://arxiv.org/abs/astro-ph/2002.06044)]. doi:10.1103/PhysRevD.102.103525.

34. Jedamzik, K.; Pogosian, L.; Zhao, G.B. Why reducing the cosmic sound horizon can not fully resolve the Hubble tension **2020**. [[arXiv:astro-ph/2010.04158](https://arxiv.org/abs/astro-ph/2010.04158)].

35. Poulin, V.; Smith, T.L.; Karwal, T.; Kamionkowski, M. Early Dark Energy Can Resolve The Hubble Tension. *Phys. Rev. Lett.* **2019**, *122*, 221301, [[arXiv:astro-ph/1811.04083](https://arxiv.org/abs/astro-ph/1811.04083)]. doi:10.1103/PhysRevLett.122.221301.

36. Niedermann, F.; Sloth, M.S. New early dark energy. *Phys. Rev. D* **2021**, *103*, L041303, [[arXiv:astro-ph/1910.10739](https://arxiv.org/abs/astro-ph/1910.10739)]. doi:10.1103/PhysRevD.103.L041303.

37. Smith, T.L.; Lucca, M.; Poulin, V.; Abellán, G.F.; Balkenhol, L.; Benabed, K.; Galli, S.; Murgia, R. Hints of Early Dark Energy in Planck, SPT, and ACT data: new physics or systematics? **2022**. [[arXiv:astro-ph/2202.09379](https://arxiv.org/abs/astro-ph/2202.09379)].

38. Smith, T.L.; Poulin, V.; Bernal, J.L.; Boddy, K.K.; Kamionkowski, M.; Murgia, R. Early dark energy is not excluded by current large-scale structure data **2020**. [[arXiv:astro-ph/2009.10740](https://arxiv.org/abs/astro-ph/2009.10740)].

39. Chudaykin, A.; Gorbunov, D.; Nedelko, N. Combined analysis of Planck and SPTPol data favors the early dark energy models. *JCAP* **2020**, *08*, 013, [[arXiv:astro-ph/2004.13046](https://arxiv.org/abs/astro-ph/2004.13046)]. doi:10.1088/1475-7516/2020/08/013.

40. Fondi, E.; Melchiorri, A.; Pagano, L. No evidence for EDE from Planck data in extended scenarios. *Astrophys. J. Lett.* **2022**, *931*, L18, [[arXiv:astro-ph/2203.12930](https://arxiv.org/abs/astro-ph/2203.12930)].

41. Sabla, V.I.; Caldwell, R.R. The Microphysics of Early Dark Energy **2022**. [[arXiv:astro-ph/2202.08291](https://arxiv.org/abs/astro-ph/2202.08291)].

42. Herold, L.; Ferreira, E.G.M.; Komatsu, E. New Constraint on Early Dark Energy from Planck and BOSS Data Using the Profile Likelihood. *Astrophys. J. Lett.* **2022**, *929*, L16, [[arXiv:astro-ph/2112.12140](https://arxiv.org/abs/astro-ph/2112.12140)]. doi:10.3847/2041-8213/ac63a3.

43. McDonough, E.; Lin, M.X.; Hill, J.C.; Hu, W.; Zhou, S. Early dark sector, the Hubble tension, and the swampland. *Phys. Rev. D* **2022**, *106*, 043525, [[arXiv:astro-ph/2112.09128](https://arxiv.org/abs/astro-ph/2112.09128)]. doi:10.1103/PhysRevD.106.043525.

44. Hill, J.C.; McDonough, E.; Toomey, M.W.; Alexander, S. Early Dark Energy Does Not Restore Cosmological Concordance **2020**. [[arXiv:astro-ph/2003.07355](https://arxiv.org/abs/astro-ph/2003.07355)].

45. Sakstein, J.; Trodden, M. Early Dark Energy from Massive Neutrinos as a Natural Resolution of the Hubble Tension. *Phys. Rev. Lett.* **2020**, *124*, 161301, [[arXiv:astro-ph/1911.11760](https://arxiv.org/abs/astro-ph/1911.11760)]. doi:10.1103/PhysRevLett.124.161301.

46. Niedermann, F.; Sloth, M.S. New Early Dark Energy is compatible with current LSS data **2020**. [[arXiv:astro-ph/2009.00006](https://arxiv.org/abs/astro-ph/2009.00006)].

47. Green, D.; et al. Messengers from the Early Universe: Cosmic Neutrinos and Other Light Relics. *Bull. Am. Astron. Soc.* **2019**, *51*, 159, [[arXiv:astro-ph/1903.04763](https://arxiv.org/abs/astro-ph/1903.04763)].

48. Schöneberg, N.; Franco Abellán, G. A step in the right direction? Analyzing the Wess Zumino Dark Radiation solution to the Hubble tension **2022**. [[arXiv:astro-ph/2206.11276](https://arxiv.org/abs/astro-ph/2206.11276)].

49. Seto, O.; Toda, Y. Comparing early dark energy and extra radiation solutions to the Hubble tension with BBN **2021**. [[arXiv:astro-ph/2101.03740](https://arxiv.org/abs/astro-ph/2101.03740)].

50. Carrillo González, M.; Liang, Q.; Sakstein, J.; Trodden, M. Neutrino-Assisted Early Dark Energy: Theory and Cosmology **2020**. [[arXiv:astro-ph/2011.09895](https://arxiv.org/abs/astro-ph/2011.09895)].

51. Braglia, M.; Ballardini, M.; Finelli, F.; Koyama, K. Early modified gravity in light of the  $H_0$  tension and LSS data. *Phys. Rev. D* **2021**, *103*, 043528, [[arXiv:astro-ph/2011.12934](https://arxiv.org/abs/astro-ph/2011.12934)]. doi:10.1103/PhysRevD.103.043528.

52. Abadi, T.; Kovetz, E.D. Can conformally coupled modified gravity solve the Hubble tension? *Phys. Rev. D* **2021**, *103*, 023530, [[arXiv:astro-ph/2011.13853](https://arxiv.org/abs/astro-ph/2011.13853)]. doi:10.1103/PhysRevD.103.023530.

53. Renk, J.; Zumalacárregui, M.; Montanari, F.; Barreira, A. Galileon gravity in light of ISW, CMB, BAO and  $H_0$  data. *JCAP* **2017**, *1710*, 020, [[arXiv:astro-ph/1707.02263](https://arxiv.org/abs/astro-ph/1707.02263)]. doi:10.1088/1475-7516/2017/10/020.

54. Nojiri, S.; Odintsov, S.D.; Oikonomou, V.K. Integral F(R) gravity and saddle point condition as a remedy for the  $H_0$ -tension. *Nucl. Phys. B* **2022**, *980*, 115850, [[arXiv:gr-qc/2205.11681](https://arxiv.org/abs/gr-qc/2205.11681)]. doi:10.1016/j.nuclphysb.2022.115850.

55. Lin, M.X.; Raveri, M.; Hu, W. Phenomenology of Modified Gravity at Recombination. *Phys. Rev.* **2019**, *D99*, 043514, [[arXiv:astro-ph/1810.02333](https://arxiv.org/abs/astro-ph/1810.02333)]. doi:10.1103/PhysRevD.99.043514.

56. Saridakis, E.N.; et al. Modified Gravity and Cosmology: An Update by the CANTATA Network **2021**. [[arXiv:gr-qc/2105.12582](#)].

57. Benisty, D. Quantifying the  $S_8$  tension with the Redshift Space Distortion data set. *Phys. Dark Univ.* **2021**, *31*, 100766, [[arXiv:astro-ph.CO/2005.03751](#)]. doi:10.1016/j.dark.2020.100766.

58. Heymans, C.; et al. KiDS-1000 Cosmology: Multi-probe weak gravitational lensing and spectroscopic galaxy clustering constraints. *Astron. Astrophys.* **2021**, *646*, A140, [[arXiv:astro-ph.CO/2007.15632](#)]. doi:10.1051/0004-6361/202039063.

59. Kazantzidis, L.; Perivolaropoulos, L. Evolution of the  $f\sigma_8$  tension with the Planck15/CDM determination and implications for modified gravity theories. *Phys. Rev. D* **2018**, *97*, 103503, [[arXiv:astro-ph.CO/1803.01337](#)]. doi:10.1103/PhysRevD.97.103503.

60. Joudaki, S.; et al. KiDS-450 + 2dFLenS: Cosmological parameter constraints from weak gravitational lensing tomography and overlapping redshift-space galaxy clustering. *Mon. Not. Roy. Astron. Soc.* **2018**, *474*, 4894–4924, [[arXiv:astro-ph.CO/1707.06627](#)]. doi:10.1093/mnras/stx2820.

61. Kazantzidis, L.; Perivolaropoulos, L.  $\sigma_8$  Tension. Is Gravity Getting Weaker at Low  $z$ ? Observational Evidence and Theoretical Implications **2019**. [[arXiv:astro-ph.CO/1907.03176](#)]. doi:10.1007/978-3-030-83715-0\_33.

62. Skara, F.; Perivolaropoulos, L. Tension of the  $E_G$  statistic and redshift space distortion data with the Planck -  $\Lambda$ CDM model and implications for weakening gravity. *Phys. Rev. D* **2020**, *101*, 063521, [[arXiv:astro-ph.CO/1911.10609](#)]. doi:10.1103/PhysRevD.101.063521.

63. Avila, F.; Bernui, A.; Bonilla, A.; Nunes, R.C. Inferring  $S_8(z)$  and  $\gamma(z)$  with cosmic growth rate measurements using machine learning. *Eur. Phys. J. C* **2022**, *82*, 594, [[arXiv:astro-ph.CO/2201.07829](#)]. doi:10.1140/epjc/s10052-022-10561-0.

64. Köhlinger, F.; et al. KiDS-450: The tomographic weak lensing power spectrum and constraints on cosmological parameters. *Mon. Not. Roy. Astron. Soc.* **2017**, *471*, 4412–4435, [[arXiv:astro-ph.CO/1706.02892](#)]. doi:10.1093/mnras/stx1820.

65. Nunes, R.C.; Vagnozzi, S. Arbitrating the  $S_8$  discrepancy with growth rate measurements from redshift-space distortions. *Mon. Not. Roy. Astron. Soc.* **2021**, *505*, 5427–5437, [[arXiv:astro-ph.CO/2106.01208](#)]. doi:10.1093/mnras/stab1613.

66. Clark, S.J.; Vattis, K.; Fan, J.; Koushiappas, S.M. The  $H_0$  and  $S_8$  tensions necessitate early and late time changes to  $\Lambda$ CDM **2021**. [[arXiv:astro-ph.CO/2110.09562](#)].

67. Ivanov, M.M.; McDonough, E.; Hill, J.C.; Simonović, M.; Toomey, M.W.; Alexander, S.; Zaldarriaga, M. Constraining Early Dark Energy with Large-Scale Structure. *Phys. Rev. D* **2020**, *102*, 103502, [[arXiv:astro-ph.CO/2006.11235](#)]. doi:10.1103/PhysRevD.102.103502.

68. Hill, J.C.; et al. Atacama Cosmology Telescope: Constraints on prerecombination early dark energy. *Phys. Rev. D* **2022**, *105*, 123536, [[arXiv:astro-ph.CO/2109.04451](#)]. doi:10.1103/PhysRevD.105.123536.

69. Vagnozzi, S. Consistency tests of  $\Lambda$ CDM from the early integrated Sachs-Wolfe effect: Implications for early-time new physics and the Hubble tension. *Phys. Rev. D* **2021**, *104*, 063524, [[arXiv:astro-ph.CO/2105.10425](#)]. doi:10.1103/PhysRevD.104.063524.

70. Philcox, O.H.E.; Farren, G.S.; Sherwin, B.D.; Baxter, E.J.; Brout, D.J. Determining the Hubble Constant without the Sound Horizon: A 3.6% Constraint on  $H_0$  from Galaxy Surveys, CMB Lensing and Supernovae **2022**. [[arXiv:astro-ph.CO/2204.02984](#)].

71. Chudaykin, A.; Gorbunov, D.; Nedelko, N. Exploring an early dark energy solution to the Hubble tension with Planck and SPTPol data. *Phys. Rev. D* **2021**, *103*, 043529, [[arXiv:astro-ph.CO/2011.04682](#)]. doi:10.1103/PhysRevD.103.043529.

72. Reeves, A.; Herold, L.; Vagnozzi, S.; Sherwin, B.D.; Ferreira, E.G.M. Restoring cosmological concordance with early dark energy and massive neutrinos? **2022**. [[arXiv:astro-ph.CO/2207.01501](#)].

73. Solà Peracaula, J.; Gómez-Valent, A.; de Cruz Pérez, J.; Moreno-Pulido, C. Brans–Dicke cosmology with a  $\Lambda$ -term: a possible solution to  $\Lambda$ CDM tensions. *Class. Quant. Grav.* **2020**, *37*, 245003, [[arXiv:astro-ph.CO/2006.04273](#)]. doi:10.1088/1361-6382/abbc43.

74. Braglia, M.; Ballardini, M.; Emond, W.T.; Finelli, F.; Gumrukcuoglu, A.E.; Koyama, K.; Paoletti, D. Larger value for  $H_0$  by an evolving gravitational constant. *Phys. Rev. D* **2020**, *102*, 023529, [[arXiv:astro-ph.CO/2004.11161](#)]. doi:10.1103/PhysRevD.102.023529.

75. Pogosian, L.; Raveri, M.; Koyama, K.; Martinelli, M.; Silvestri, A.; Zhao, G.B. Imprints of cosmological tensions in reconstructed gravity **2021**. [[arXiv:astro-ph.CO/2107.12992](#)].

76. Bahamonde, S.; Dialektopoulos, K.F.; Escamilla-Rivera, C.; Farrugia, G.; Gakis, V.; Hendry, M.; Hohmann, M.; Said, J.L.; Mifsud, J.; Di Valentino, E. Teleparallel Gravity: From Theory to Cosmology **2021**. [[arXiv:gr-qc/2106.13793](#)].

77. Di Valentino, E.; Mukherjee, A.; Sen, A.A. Dark Energy with Phantom Crossing and the  $H_0$  Tension. *Entropy* **2021**, *23*, 404, [[arXiv:astro-ph.CO/2005.12587](#)]. doi:10.3390/e23040404.

78. Alestas, G.; Kazantzidis, L.; Perivolaropoulos, L.  $H_0$  Tension, Phantom Dark Energy and Cosmological Parameter Degeneracies. *Phys. Rev. D* **2020**, *101*, 123516, [[arXiv:astro-ph.CO/2004.08363](#)]. doi:10.1103/PhysRevD.101.123516.

79. Di Valentino, E.; Melchiorri, A.; Mena, O.; Vagnozzi, S. Nonminimal dark sector physics and cosmological tensions. *Phys. Rev. D* **2020**, *101*, 063502, [[arXiv:astro-ph.CO/1910.09853](#)]. doi:10.1103/PhysRevD.101.063502.

80. Pan, S.; Yang, W.; Di Valentino, E.; Shafieloo, A.; Chakraborty, S. Reconciling  $H_0$  tension in a six parameter space? *JCAP* **2020**, *06*, 062, [[arXiv:astro-ph.CO/1907.12551](#)]. doi:10.1088/1475-7516/2020/06/062.

81. Li, X.; Shafieloo, A. A Simple Phenomenological Emergent Dark Energy Model can Resolve the Hubble Tension. *Astrophys. J. Lett.* **2019**, *883*, L3, [[arXiv:astro-ph.CO/1906.08275](#)]. doi:10.3847/2041-8213/ab3e09.

82. Zhao, G.B.; et al. Dynamical dark energy in light of the latest observations. *Nature Astron.* **2017**, *1*, 627–632, [[arXiv:astro-ph.CO/1701.08165](#)]. doi:10.1038/s41550-017-0216-z.

83. Keeley, R.E.; Joudaki, S.; Kaplinghat, M.; Kirkby, D. Implications of a transition in the dark energy equation of state for the  $H_0$  and  $\sigma_8$  tensions. *JCAP* **2019**, *12*, 035, [[arXiv:astro-ph.CO/1905.10198](#)]. doi:10.1088/1475-7516/2019/12/035.

84. Sola Peracaula, J.; Gomez-Valent, A.; de Cruz Pérez, J. Signs of Dynamical Dark Energy in Current Observations. *Phys. Dark Univ.* **2019**, *25*, 100311, [[arXiv:astro-ph.CO/1811.03505](#)]. doi:10.1016/j.dark.2019.100311.

85. Yang, W.; Pan, S.; Di Valentino, E.; Saridakis, E.N.; Chakraborty, S. Observational constraints on one-parameter dynamical dark-energy parametrizations and the  $H_0$  tension. *Phys. Rev.* **2019**, *D99*, 043543, [[arXiv:astro-ph.CO/1810.05141](#)]. doi:10.1103/PhysRevD.99.043543.

86. Di Valentino, E.; Melchiorri, A.; Mena, O.; Vagnozzi, S. Interacting dark energy in the early 2020s: A promising solution to the  $H_0$  and cosmic shear tensions. *Phys. Dark Univ.* **2020**, *30*, 100666, [[arXiv:astro-ph.CO/1908.04281](#)]. doi:10.1016/j.dark.2020.100666.

87. Yang, W.; Pan, S.; Di Valentino, E.; Nunes, R.C.; Vagnozzi, S.; Mota, D.F. Tale of stable interacting dark energy, observational signatures, and the  $H_0$  tension. *JCAP* **2018**, *1809*, 019, [[arXiv:astro-ph.CO/1805.08252](#)]. doi:10.1088/1475-7516/2018/09/019.

88. Vattis, K.; Koushiappas, S.M.; Loeb, A. Dark matter decaying in the late Universe can relieve the  $H_0$  tension. *Phys. Rev.* **2019**, *D99*, 121302, [[arXiv:astro-ph.CO/1903.06220](#)]. doi:10.1103/PhysRevD.99.121302.

89. Yang, W.; Mukherjee, A.; Di Valentino, E.; Pan, S. Interacting dark energy with time varying equation of state and the  $H_0$  tension. *Phys. Rev.* **2018**, *D98*, 123527, [[arXiv:astro-ph.CO/1809.06883](#)]. doi:10.1103/PhysRevD.98.123527.

90. Ghosh, S.; Khatri, R.; Roy, T.S. Can dark neutrino interactions phase out the Hubble tension? *Phys. Rev. D* **2020**, *102*, 123544, [[arXiv:hep-ph/1908.09843](#)]. doi:10.1103/PhysRevD.102.123544.

91. Alestas, G.; Perivolaropoulos, L. Late time approaches to the Hubble tension deforming  $H(z)$ , worsen the growth tension. *Mon. Not. Roy. Astron. Soc.* **2021**, *504*, 3956, [[arXiv:astro-ph.CO/2103.04045](#)]. doi:10.1093/mnras/stab1070.

92. Keeley, R.E.; Shafieloo, A. Ruling Out New Physics at Low Redshift as a solution to the  $H_0$  Tension **2022**. [[arXiv:astro-ph.CO/2206.08440](#)].

93. Clark, S.J.; Vattis, K.; Koushiappas, S.M. CMB constraints on late-universe decaying dark matter as a solution to the  $H_0$  tension **2020**. [[arXiv:astro-ph.CO/2006.03678](#)].

94. Chen, A.; et al. Constraints on dark matter to dark radiation conversion in the late universe with DES-Y1 and external data. *Phys. Rev. D* **2021**, *103*, 123528, [[arXiv:astro-ph.CO/2011.04606](#)]. doi:10.1103/PhysRevD.103.123528.

95. Anchordoqui, L.A.; Barger, V.; Marfatia, D.; Soriano, J.F. Decay of multiple dark matter particles to dark radiation in different epochs does not alleviate the Hubble tension. *Phys. Rev. D* **2022**, *105*, 103512, [[arXiv:astro-ph.CO/2203.04818](#)]. doi:10.1103/PhysRevD.105.103512.

96. Mau, S.; et al. Milky Way Satellite Census. IV. Constraints on Decaying Dark Matter from Observations of Milky Way Satellite Galaxies. *Astrophys. J.* **2022**, *932*, 128, [[arXiv:astro-ph.CO/2201.11740](#)]. doi:10.3847/1538-4357/ac6e65.

97. Cai, R.G.; Guo, Z.K.; Wang, S.J.; Yu, W.W.; Zhou, Y. No-go guide for the Hubble tension : matter perturbations **2022**. [[arXiv:astro-ph.CO/2202.12214](#)].

98. Heisenberg, L.; Villarrubia-Rojo, H.; Zosso, J. Can late-time extensions solve the  $H_0$  and  $\sigma_8$  tensions? *Phys. Rev. D* **2022**, *106*, 043503, [[arXiv:astro-ph.CO/2202.01202](#)]. doi:10.1103/PhysRevD.106.043503.

99. Vagnozzi, S.; Pacucci, F.; Loeb, A. Implications for the Hubble tension from the ages of the oldest astrophysical objects. *JHEAp* **2022**, *36*, 27–35, [[arXiv:astro-ph.CO/2105.10421](#)]. doi:10.1016/j.jheap.2022.07.004.

100. Alam, S.; et al. Completed SDSS-IV extended Baryon Oscillation Spectroscopic Survey: Cosmological implications from two decades of spectroscopic surveys at the Apache Point Observatory. *Phys. Rev. D* **2021**, *103*, 083533, [[arXiv:astro-ph.CO/2007.08991](#)]. doi:10.1103/PhysRevD.103.083533.

101. Mortsell, E.; Goobar, A.; Johansson, J.; Dhawan, S. The Hubble Tension Bites the Dust: Sensitivity of the Hubble Constant Determination to Cepheid Color Calibration **2021**. [[arXiv:astro-ph.CO/2105.11461](#)].

102. Efstathiou, G.  $H_0$  Revisited. *Mon. Not. Roy. Astron. Soc.* **2014**, *440*, 1138–1152, [[arXiv:astro-ph.CO/1311.3461](#)]. doi:10.1093/mnras/stu278.

103. Efstathiou, G. A Lockdown Perspective on the Hubble Tension (with comments from the SH0ES team) **2020**. [[arXiv:astro-ph.CO/2007.10716](#)].

104. Efstathiou, G. To  $H_0$  or not to  $H_0$ ? **2021**. [[arXiv:astro-ph.CO/2103.08723](#)].

105. Wojtak, R.; Hjorth, J. Intrinsic tension in the supernova sector of the local Hubble constant measurement and its implications **2022**. [[arXiv:astro-ph.CO/2206.08160](#)]. doi:10.1093/mnras/stac1878.

106. Kenworthy, W.D.; Scolnic, D.; Riess, A. The Local Perspective on the Hubble Tension: Local Structure Does Not Impact Measurement of the Hubble Constant. *Astrophys. J.* **2019**, *875*, 145, [[arXiv:astro-ph.CO/1901.08681](#)]. doi:10.3847/1538-4357/ab0ebf.

107. Riess, A.G.; Breuval, L.; Yuan, W.; Casertano, S.; Macri, L.M.; Scolnic, D.; Cantat-Gaudin, T.; Anderson, R.I.; Reyes, M.C. Cluster Cepheids with High Precision Gaia Parallaxes, Low Zeropoint Uncertainties, and Hubble Space Telescope Photometry **2022**. [[arXiv:astro-ph.CO/2208.01045](#)].

108. Yuan, W.; Macri, L.M.; Riess, A.G.; Brink, T.G.; Casertano, S.; Filippenko, A.V.; Hoffmann, S.L.; Huang, C.D.; Scolnic, D. Absolute Calibration of Cepheid Period-Luminosity Relations in NGC 4258 **2022**. [[arXiv:astro-ph.GA/2203.06681](#)].

109. Riess, A.G.; et al. Milky Way Cepheid Standards for Measuring Cosmic Distances and Application to Gaia DR2: Implications for the Hubble Constant. *Astrophys. J.* **2018**, *861*, 126, [[arXiv:astro-ph.CO/1804.10655](#)]. doi:10.3847/1538-4357/aac82e.

110. Alestas, G.; Camarena, D.; Di Valentino, E.; Kazantzidis, L.; Marra, V.; Nesseris, S.; Perivolaropoulos, L. Late-transition versus smooth H(z)-deformation models for the resolution of the Hubble crisis. *Phys. Rev. D* **2022**, *105*, 063538, [[arXiv:astro-ph.CO/2110.04336](https://arxiv.org/abs/2110.04336)]. doi:10.1103/PhysRevD.105.063538.

111. Desmond, H.; Jain, B.; Sakstein, J. Local resolution of the Hubble tension: The impact of screened fifth forces on the cosmic distance ladder. *Phys. Rev.* **2019**, *D100*, 043537, [[arXiv:astro-ph.CO/1907.03778](https://arxiv.org/abs/1907.03778)]. doi:10.1103/PhysRevD.100.043537.

112. Perivolaropoulos, L.; Skara, F. Hubble tension or a transition of the Cepheid SNIa calibrator parameters? *Phys. Rev. D* **2021**, *104*, 123511, [[arXiv:astro-ph.CO/2109.04406](https://arxiv.org/abs/2109.04406)]. doi:10.1103/PhysRevD.104.123511.

113. Odintsov, S.D.; Oikonomou, V.K. Did the Universe experience a pressure non-crushing type cosmological singularity in the recent past? *EPL* **2022**, *137*, 39001, [[arXiv:gr-qc/2201.07647](https://arxiv.org/abs/2201.07647)]. doi:10.1209/0295-5075/ac52dc.

114. Alestas, G.; Kazantzidis, L.; Perivolaropoulos, L.  $w - M$  phantom transition at  $z_t < 0.1$  as a resolution of the Hubble tension. *Phys. Rev. D* **2021**, *103*, 083517, [[arXiv:astro-ph.CO/2012.13932](https://arxiv.org/abs/2012.13932)]. doi:10.1103/PhysRevD.103.083517.

115. Marra, V.; Perivolaropoulos, L. A rapid transition of  $G_{\text{eff}}$  at  $z_t \simeq 0.01$  as a possible solution of the Hubble and growth tensions. *Phys. Rev. D* **2021**, *104*, L021303, [[arXiv:astro-ph.CO/2102.06012](https://arxiv.org/abs/2102.06012)]. doi:10.1103/PhysRevD.104.L021303.

116. Alestas, G.; Antoniou, I.; Perivolaropoulos, L. Hints for a gravitational constant transition in Tully-Fisher data **2021**. [[arXiv:astro-ph.CO/2104.14481](https://arxiv.org/abs/2104.14481)].

117. Perivolaropoulos, L. Is the Hubble Crisis Connected with the Extinction of Dinosaurs? *Universe* **2022**, *8*, 263, [[arXiv:astro-ph.EP/2201.08997](https://arxiv.org/abs/astro-ph.EP/2201.08997)]. doi:10.3390/universe8050263.

118. Perivolaropoulos, L.; Skara, F. Gravitational transitions via the explicitly broken symmetron screening mechanism **2022**. [[arXiv:astro-ph.CO/2203.10374](https://arxiv.org/abs/2203.10374)].

119. Riess, A.G.; et al. A 2.4% Determination of the Local Value of the Hubble Constant. *Astrophys. J.* **2016**, *826*, 56, [[arXiv:astro-ph.CO/1604.01424](https://arxiv.org/abs/1604.01424)]. doi:10.3847/0004-637X/826/1/56.

120. Riess, A.G.; Casertano, S.; Yuan, W.; Macri, L.M.; Scolnic, D. Large Magellanic Cloud Cepheid Standards Provide a 1% Foundation for the Determination of the Hubble Constant and Stronger Evidence for Physics beyond  $\Lambda$ CDM. *Astrophys. J.* **2019**, *876*, 85, [[arXiv:astro-ph.CO/1903.07603](https://arxiv.org/abs/1903.07603)]. doi:10.3847/1538-4357/ab1422.

121. Riess, A.G.; Casertano, S.; Yuan, W.; Bowers, J.B.; Macri, L.; Zinn, J.C.; Scolnic, D. Cosmic Distances Calibrated to 1% Precision with Gaia EDR3 Parallaxes and Hubble Space Telescope Photometry of 75 Milky Way Cepheids Confirm Tension with  $\Lambda$ CDM. *Astrophys. J. Lett.* **2021**, *908*, L6, [[arXiv:astro-ph.CO/2012.08534](https://arxiv.org/abs/2012.08534)]. doi:10.3847/2041-8213/abdbaf.

122. Reid, M.; Pesce, D.; Riess, A. An Improved Distance to NGC 4258 and its Implications for the Hubble Constant. *Astrophys. J. Lett.* **2019**, *886*, L27, [[arXiv:astro-ph.GA/1908.05625](https://arxiv.org/abs/1908.05625)]. doi:10.3847/2041-8213/ab552d.

123. Li, S.; Riess, A.G.; Busch, M.P.; Casertano, S.; Macri, L.M.; Yuan, W. A sub-2% Distance to M31 from Photometrically Homogeneous Near-Infrared Cepheid Period-Luminosity Relations Measured with the Hubble Space Telescope **2021**. [[arXiv:astro-ph.CO/2107.08029](https://arxiv.org/abs/2107.08029)].

124. Madore, B.F. The period-luminosity relation. IV. Intrinsic relations and reddening for the Large Magellanic Cloud Cepheids. *Astroph. J.* **1982**, *253*, 575–579. doi:10.1086/159659.

125. Fitzpatrick, E.L. Correcting for the effects of interstellar extinction. *Publ. Astron. Soc. Pac.* **1999**, *111*, 63–75, [[astro-ph/9809387](https://arxiv.org/abs/astro-ph/9809387)]. doi:10.1086/316293.

126. Camarena, D.; Marra, V. On the use of the local prior on the absolute magnitude of Type Ia supernovae in cosmological inference. *Mon. Not. Roy. Astron. Soc.* **2021**, *504*, 5164–5171, [[arXiv:astro-ph.CO/2101.08641](https://arxiv.org/abs/2101.08641)]. doi:10.1093/mnras/stab1200.

127. Gómez-Valent, A. Measuring the sound horizon and absolute magnitude of SNIa by maximizing the consistency between low-redshift data sets. *Phys. Rev. D* **2022**, *105*, 043528, [[arXiv:astro-ph.CO/2111.15450](https://arxiv.org/abs/2111.15450)]. doi:10.1103/PhysRevD.105.043528.

128. Kerscher, M.; Weller, J. On Model Selection in Cosmology. *SciPost Phys. Lect. Notes* **2019**, *9*, 1, [[arXiv:astro-ph.CO/1901.07726](https://arxiv.org/abs/1901.07726)]. doi:10.21468/SciPostPhysLectNotes.9.

129. Liddle, A.R. Information criteria for astrophysical model selection. *Mon. Not. Roy. Astron. Soc.* **2007**, *377*, L74–L78, [[arXiv:astro-ph/0701113](https://arxiv.org/abs/astro-ph/0701113)]. doi:10.1111/j.1745-3933.2007.00306.x.

130. Akaike, H. A new look at the statistical model identification. *IEEE Transactions on Automatic Control* **1974**, *19*, 716–723.

131. Freedman, W.L.; et al. The Carnegie-Chicago Hubble Program. VIII. An Independent Determination of the Hubble Constant Based on the Tip of the Red Giant Branch **2019**. [[arXiv:astro-ph.CO/1907.05922](https://arxiv.org/abs/1907.05922)]. doi:10.3847/1538-4357/ab2f73.

132. Coleman, S.R. The Fate of the False Vacuum. 1. Semiclassical Theory. *Phys. Rev. D* **1977**, *15*, 2929–2936. [Erratum: *Phys. Rev. D* **16**, 1248 (1977)], doi:10.1103/PhysRevD.16.1248.

133. Callan, Jr., C.G.; Coleman, S.R. The Fate of the False Vacuum. 2. First Quantum Corrections. *Phys. Rev. D* **1977**, *16*, 1762–1768. doi:10.1103/PhysRevD.16.1762.

134. Patwardhan, A.V.; Fuller, G.M. Late-time vacuum phase transitions: Connecting sub-eV scale physics with cosmological structure formation. *Phys. Rev. D* **2014**, *90*, 063009, [[arXiv:astro-ph.CO/1401.1923](https://arxiv.org/abs/1401.1923)]. doi:10.1103/PhysRevD.90.063009.

135. Niedermann, F.; Sloth, M.S. Resolving the Hubble tension with new early dark energy. *Phys. Rev. D* **2020**, *102*, 063527, [[arXiv:astro-ph.CO/2006.06686](https://arxiv.org/abs/2006.06686)]. doi:10.1103/PhysRevD.102.063527.

136. Liddle, A.R. How many cosmological parameters? *Mon. Not. Roy. Astron. Soc.* **2004**, *351*, L49–L53, [[arXiv:astro-ph/astro-ph/0401198](https://arxiv.org/abs/astro-ph/0401198)]. doi:10.1111/j.1365-2966.2004.08033.x.

137. Arevalo, F.; Cid, A.; Moya, J. AIC and BIC for cosmological interacting scenarios. *Eur. Phys. J.* **2017**, *C77*, 565, [[arXiv:astro-ph.CO/1610.09330](https://arxiv.org/abs/astro-ph.CO/1610.09330)]. doi:10.1140/epjc/s10052-017-5128-7.

138. Schwarz, G. Estimating the Dimension of a Model. *Annals Statist.* **1978**, *6*, 461–464.

139. John, M.V.; Narlikar, J.V. Comparison of cosmological models using bayesian theory. *Phys. Rev. D* **2002**, *65*, 043506, [[astro-ph/0111122](https://arxiv.org/abs/astro-ph/0111122)]. doi:10.1103/PhysRevD.65.043506.

140. Nesseris, S.; Garcia-Bellido, J. Is the Jeffreys’ scale a reliable tool for Bayesian model comparison in cosmology? *JCAP* **2013**, *08*, 036, [[arXiv:astro-ph.CO/1210.7652](https://arxiv.org/abs/astro-ph.CO/1210.7652)]. doi:10.1088/1475-7516/2013/08/036.

141. Jeffreys, H. *Theory of probability*, 3 ed.; Oxford University Press, 1961.

142. Bonilla Rivera, A.; García-Farieta, J.E. Exploring the Dark Universe: constraints on dynamical Dark Energy models from CMB, BAO and growth rate measurements. *Int. J. Mod. Phys. D* **2019**, *28*, 1950118, [[arXiv:astro-ph.CO/1605.01984](https://arxiv.org/abs/astro-ph.CO/1605.01984)]. doi:10.1142/S0218271819501189.

143. Pérez-Romero, J.; Nesseris, S. Cosmological constraints and comparison of viable  $f(R)$  models. *Phys. Rev. D* **2018**, *97*, 023525, [[arXiv:astro-ph.CO/1710.05634](https://arxiv.org/abs/astro-ph.CO/1710.05634)]. doi:10.1103/PhysRevD.97.023525.

144. Camarena, D.; Marra, V. Impact of the cosmic variance on  $H_0$  on cosmological analyses. *Phys. Rev. D* **2018**, *98*, 023537, [[arXiv:astro-ph.CO/1805.09900](https://arxiv.org/abs/astro-ph.CO/1805.09900)]. doi:10.1103/PhysRevD.98.023537.

145. Rezaei, M.; Malekjani, M.; Sola, J. Can dark energy be expressed as a power series of the Hubble parameter? *Phys. Rev. D* **2019**, *100*, 023539, [[arXiv:gr-qc/1905.00100](https://arxiv.org/abs/gr-qc/1905.00100)]. doi:10.1103/PhysRevD.100.023539.